Phenology-Based Backscattering Model for Corn at L-Band

Alejandro Monsivais-Huertero⬤, *Senior Member, IEEE*, Pang-Wei Liu, *Member, IEEE*, and Jasmeet Judge, *Senior Member, IEEE*

Abstract—In this paper, we developed and evaluated a phenology-based coherent scattering model to estimate terrain backscatter at the L-band for growing corn. The scattering model accounted for combined effects from periodicity in soil and vegetation, and changes in plant structure and phenology. The model estimates were compared with observations during the two growing seasons in North Central Florida. The unbiased average root-mean-square (rms) differences between the model and observations decreased from 5 to 1.31 dB when these combined effects were included. During the early stage, direct scattering from soil was the primary scattering mechanism, and as the vegetation increased, the interactions between stems and soil became the dominant scattering mechanism. The most sensitive soil parameters were moisture content and rms height, and vegetation parameters were the widths of stems, leaves, and ears, and the stem water content. This paper demonstrates that it is necessary to consider periodicity and plant structural effects in algorithms to retrieve realistic soil moisture in agricultural terrain.

Index Terms—Coherent scattering model, periodic surface, phenology-based backscatter model.

I. Introduction

SOIL moisture (SM) is an important land surface variable for understanding the water cycle, ecosystem productivity, and linkages between water, energy, and carbon cycles. Low microwave frequencies, particularly at <10 GHz, are highly sensitive to moisture in the upper few centimeters of the soil [1], [2]. For SM studies, observations at L-band frequencies of 1.2–1.4 GHz are more desirable than higher frequencies due to larger penetration depths. Currently, the operational satellite-based microwave sensors at the L-band, such as the Phased Array L-band Synthetic Aperture Radar in the Second Advanced Land Observing Satellite (ALOS/PALSAR-2) [3]–[5], the European Space Agency's Soil Moisture and Ocean Salinity [6], and the NASA Soil Moisture

A. Monsivais-Huertero is with the Escuela Superior de Ingenieria Mecanica y Electrica Unidad Ticoman, Instituto Politecnico Nacional, Mexico City 07340, Mexico (e-mail: amonsiva@ipn.mx).

P.-W. Liu is with the National Aeronautics and Space Administration's Jet Propulsion Laboratory, California Institute of Technology, Pasadena, CA 91125 USA.

J. Judge is with the Center for Remote Sensing, Department of Agricultural and Biological Engineering, University of Florida, Gainesville, FL 32611 USA.

Active/Passive (SMAP) [7] missions, collect data for global monitoring of SM. The SMAP mission [7] included active and passive sensors at the L-band to provide global observations of SM, with a repeated coverage of every 2–3 days from April to July 2015. In addition, three new satellites with an SAR at the L-band, viz., the Argentinean–Italian SAOCOM 1A and 1B [8] to be launched in 2017 and 2018, respectively, and the NASA-ISRO SAR mission [9] scheduled to launch in 2020. Both the active (radar) and passive (radiometer) microwave sensors measure radiation quantities that are functions of soil dielectric constant and exhibit similar sensitivities to SM. Active and/or passive observations have been used to improve SM through downscaling [2], [10]–[13], optimization [14]–[18], and assimilation frameworks [19]–[22]. While a significant progress has been made in developing and validating forward models for passive studies, active forward models have been less studied. In addition to the SM sensitivity, radar backscatter is highly sensitive to the roughness of soil surface and scattering within the vegetation, resulting in a dynamic range in backscatter. A gap still remains in developing and validating forward models for active studies particularly under dynamic vegetation conditions [1], [2], [23]. These forward models are essential for effective assimilation and SM retrieval algorithms.

Reliable estimates of SM from active L-band observations remain challenging, because the backscatter from agricultural fields depends upon row effects from soil and vegetation, plant geometry/structure, and crop phenology. Bare-soil surfaces are generally represented as random dielectric rough surfaces. However, recent studies [23]–[25] have found differences of up to 5 dB between model simulations with random surface and actual field observations. These differences were primarily due to unaccounted periodic effects in the representation of the plowed soil as a random surface. Very few studies consider row/periodic effects from vegetation [24], [26], [27]. Whitt and Ulaby [24] and He *et al.* [28] analyzed field observations to account for the row effects in wheat and concluded that lower frequencies, such as the L-band, were more affected by row orientation than higher frequencies, such as S-, C-, and X-bands. Modeling study by Stiles *et al.* [27] showed that, for row-structured vegetation, phase-coherent effects could be significant and may be the dominant mechanism toward overall scattering at low frequencies. However, these studies were conducted for mature vegetation with a moderate level of biomass. Furthermore, studies that include combined effects of row effects in both soil and vegetation during the growing season are rare [24], [26], [29].
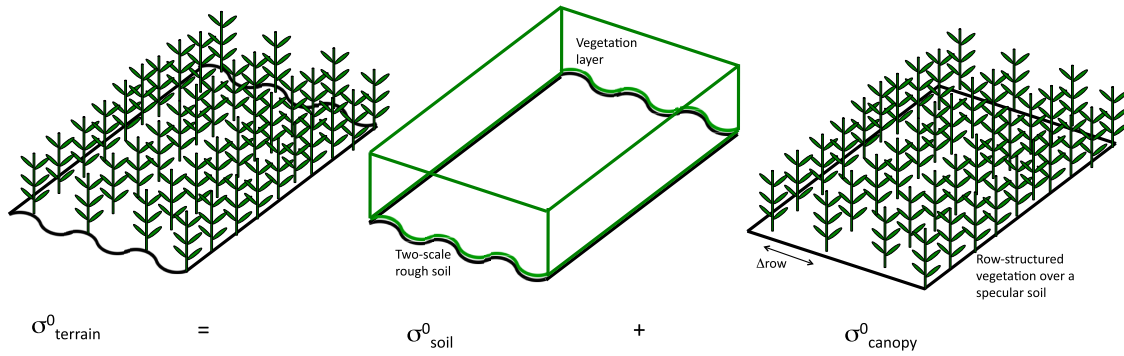
Fig. 1. Components conforming the backscatter from the corn field, $\sigma^0_{\text{terrain}}$, as expressed in (1).

Plant structure, including relative location and orientation of vegetation elements, such as leaves and stems in some crops, for example corn and wheat, can produce coherent effects that dominate incoherent effects [27], [30]. Chauhan *et al.* [30] compared coherent and incoherent approaches to understand the effect of the plant structure for corn during the mature vegetative stage with maximum biomass. They found that the coherent approach better captured geometrical effects in the modeled backscatter when compared with observations. It also identified soil–vegetation interactions as the dominant scattering mechanism. Furthermore, variations in plant structure are correlated with phenological changes during the growing season. However, only a few studies have investigated backscatter from crops over a complete growing season [23], [31], [32]. Liu *et al.* [31] studied temporal variations of dominant scattering mechanisms and demonstrated that the incorporation of the phenological characteristics of rice over different growing stages in a backscattering model reduces differences between model estimates and radar observations. Monsivais-Huertero and Judge [23] conducted a comparative study to analyze the sensitivity of an incoherent model and a coherent model to SM over a complete growing season of corn and found that a radar signature is highly dependent on the soil contribution during the early stage and to ground–vegetation–ground interactions during the reproductive stage. However, the backscatter estimated by the coherent model was about 5 dB lower than the typical values reported in the literature [12], [33]–[35], indicating the need to incorporate row effects from both soil and vegetation. Thus, a significant gap exists in understanding the combined effects of phenological changes and geometry/structural variations in the plant on dominant scattering mechanisms during the complete season of the crops, particularly in high-biomass vegetation, such as corn.

Most of the models for simulating backscatter dynamics in corn use semiempirical approaches [34]–[36] and/or semiempirical correction factors [33], [37] to account for the row effects and changes in phenology and plant structure. Differences up to 5 dB still exist between model estimates and observations. Furthermore, these studies have been restricted to limited periods within the growing season. In contrast to semiempirical approaches, physically based models can cover a wider range of season-long conditions (e.g., [2], [18], and [38] at the L-band and [1], [2], and [36] at the C-band). Most of the modeling studies have focused on understanding either the impacts of plant structure and phenological

changes or the impacts of row effects on terrain backscatter. Physically based models that account for combined effects from periodicity in soil and vegetation, phenological changes, and plant structure throughout the growing season, particularly at low microwave frequencies, can provide more realistic estimates of backscatter.

The goal of this paper is to address current knowledge gaps and understand the combined coherent effects of soil and vegetation rows, phenological changes, and plant structure on backscatter from growing sweet corn at the L-band. The specific objectives are to: 1) develop a coherent model that accounts for these effects; 2) calibrate the model during a growing season using the L-band backscatter and other field observations; and 3) evaluate the model using observations from another growing season. In this paper, we use observations from the Tenth and Eleventh Microwave Water Energy Balance Experiments (MicroWEX-10 [39] and MicroWEX-11 [40]) to develop, calibrate, and evaluate the model. The results of this paper provide insights into the dominant scattering mechanisms over the growing period and the sensitivity of the L-band backscatter to different soil and vegetation parameters for sweet corn. In Sections II–IV, we describe the active coherent model for corn, the MicroWEX-10 and MicroWEX-11 observations, and the calibration/evaluation methodology.

II. Electromagnetic Modeling

The backscatter from a corn field ($\sigma^0_{\text{terrain}}$) can be expressed as (Fig. 1)

$$\begin{aligned} \sigma^0_{\text{terrain}} &= \sigma^0_{\text{soil}} + \sigma^0_{\text{canopy}} \\ &= \sigma^0_{\text{soil}} + \sigma^0_{\text{dir}} + \sigma^0_{\text{int}} \end{aligned} \tag{1}$$

where σ^0_{soil} represents the direct backscatter contribution of the underlying row periodic soil, and σ^0_{canopy} is the backscatter from a row periodic vegetation over a specular soil and composed of σ^0_{dir} and σ^0_{int}. The σ^0_{dir} represents the direct backscatter from vegetation, and σ^0_{int} is the interactions between vegetation and soil. In this paper, σ^0_{soil} accounts for row effects by representing two components, the periodic component and the random component in the soil. The σ^0_{dir} and σ^0_{int} account for the vegetation periodicity due to the rows, the geometry/structure of the corn plants, and phenological changes. Sections II-A and II-B provide a detailed description of electromagnetic modeling to compute the three contributions.
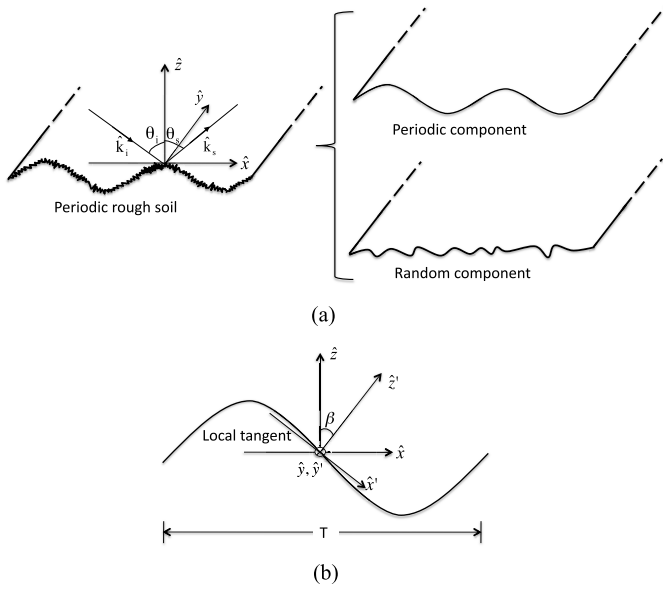
Fig. 2. (a) Components of the periodic rough soil. (b) Geometrical relationship between the global coordinate system ($\hat{x}$, $\hat{y}$, $\hat{z}$) and the local coordinate system ($\hat{x}'$, $\hat{y}'$, $\hat{z}'$) during period T.

A. Soil Contribution

A typical agricultural surface profile is composed of a large-scale periodic component due to plowing of the field and a small-scale random roughness component [Fig. 2(a)]. The backscatter from a surface at a local coordinate system is transformed into a global coordinate system [see Fig. 2(b)] based on equations presented in [24] to model the periodic component. Because the periodic behavior of the surface is assumed along the $\hat{x}$-axis, only one Eulerian angle [$\beta(x)$] is needed to relate the local coordinate system to the global coordinate system. As shown in Fig. 2(b), the equations relating the local and global coordinate systems are

$$\hat{x}' = \cos(\beta(x))\hat{x} - \sin(\beta(x))\hat{z} \tag{2a}$$
$$\hat{y}' = \hat{y} \tag{2b}$$
$$\hat{z}' = \sin(\beta(x))\hat{x} + \cos(\beta(x))\hat{z} \tag{2c}$$

where ($\hat{x}$, $\hat{y}$, $\hat{z}$) are the unit vectors of the global coordinate system. The angle $\beta(x)$ is related to the height profile of the periodic surface, $Z(x)$, by [Fig. 2(b)]

$$\tan(\beta(x)) = \frac{dZ(x)}{dx}. \tag{3}$$

Following the geometry described in Fig. 2, the incidence direction is defined by (θ_i, ϕ_i) and the scattering direction by (θ_s, ϕ_s). The incidence (θ_i', ϕ_i') and scattered (θ_s', ϕ_s') angles at the local coordinate system are given by

$$\begin{cases} \cos\theta_i' = \hat{k}_i \cdot \hat{z}' \\ \tan\phi_i' = \dfrac{\hat{k}_i \cdot \hat{y}'}{\hat{k}_i \cdot \hat{x}'} \end{cases} \tag{4}$$

$$\begin{cases} \cos\theta_s' = \hat{k}_s \cdot \hat{z}' \\ \tan\phi_s' = \dfrac{\hat{k}_s \cdot \hat{y}'}{\hat{k}_s \cdot \hat{x}'} \end{cases} \tag{5}$$

where $\hat{k}_i$ and $\hat{k}_s$ are the incident and scattered wave vectors, respectively, given by

$$\hat{k}_i = \sin\theta_i \cos\phi_i \hat{x} + \sin\theta_i \sin\phi_i \hat{y} + \cos\theta_i \hat{z} \tag{6}$$
$$\hat{k}_s = \sin\theta_s \cos\phi_s \hat{x} + \sin\theta_s \sin\phi_s \hat{y} + \cos\theta_s \hat{z}. \tag{7}$$

The polarization vectors ($\hat{v}_i$ and $\hat{h}_i$) of the incident wave and ($\hat{v}_s$ and $\hat{h}_s$) of the scattered wave are

$$\hat{h}_i = -\sin\phi_i \hat{x} + \cos\phi_i \hat{y} \tag{8a}$$
$$\hat{v}_i = \cos\theta_i \cos\phi_i \hat{x} + \cos\theta_i \sin\phi_i \hat{y} - \sin\theta_i \hat{z} \tag{8b}$$
$$\hat{h}_s = -\sin\phi_s \hat{x} + \cos\phi_s \hat{y} \tag{9a}$$
$$\hat{v}_s = \cos\theta_s \cos\phi_s \hat{x} + \cos\theta_s \sin\phi_s \hat{y} - \sin\theta_s \hat{z}. \tag{9a}$$

The polarization vectors ($\hat{v}_i'$ and $\hat{h}_i'$) of the incident wave and ($\hat{v}_s'$ and $\hat{h}_s'$) of the scattered wave at the local coordinate system are given by the same expressions by adding a prime to all the quantities in (8) and (9).

We define the transformation matrices from the local to the global coordinate system for the incident and scattered waves as

$$\mathbf{U}^s = \begin{bmatrix} \hat{v}_s \cdot \hat{v}_s' & \hat{v}_s \cdot \hat{h}_s' \\ \hat{h}_s \cdot \hat{v}_s' & \hat{h}_s \cdot \hat{h}_s' \end{bmatrix} \tag{10}$$

and

$$\mathbf{U}^i = \begin{bmatrix} \hat{v}_i' \cdot \hat{v}_i & \hat{v}_i' \cdot \hat{h}_i \\ \hat{h}_i' \cdot \hat{v}_i & \hat{h}_i' \cdot \hat{h}_i \end{bmatrix}. \tag{11}$$

The surface scattering matrix at the global coordinate system by the periodic surface over a period T is given by

$$\mathbf{S}^{\text{surface}} = \langle \mathbf{S}_{pq}\mathbf{S}_{pq}^* \rangle = \frac{1}{T}\int_0^T \langle \mathbf{Q}_{pq}\mathbf{Q}_{pq}^* \rangle dx' \tag{12}$$

with

$$\langle \mathbf{Q}_{pq}\mathbf{Q}_{pq}^* \rangle = \sum_{k,l=1}^{2} |U_{pk}^i|^2 \langle S_{kl}' S_{kl}'^* \rangle |U_{lq}^s|^2 \tag{13}$$

and

$$dx' = \sec\beta(x)dx. \tag{14}$$

In (13), $\langle S_{kl}' S_{kl}'^* \rangle$ is the scattering matrix of the random rough surface at the local coordinate system. For this paper, the scattering matrix of a random rough surface is calculated using the advanced integral equation method (AIEM) [41], [42].

The soil contribution (σ_{soil}^0) of (1) can be computed by

$$\sigma_{\text{soil},pq}^0 = 4\pi \cos\theta_s |\mathbf{S}_{pq}^{\text{soil}}|^2 \tag{15}$$

where $\{p,q\} = \{V,H\}$ and $\mathbf{S}^{\text{soil}}$ is given by

$$\mathbf{S}^{\text{soil}} = \mathbf{T}^t \cdot \mathbf{S}^{\text{surface}} \cdot \mathbf{T}^t \tag{16}$$

with T^t representing the transmissivity matrix for the total path when the EM wave travels within the vegetation layer as explained in (37) (see Section II-B2). In the case of bare-soil conditions, $\mathbf{S}^{\text{soil}} = \mathbf{S}^{\text{surface}}$.

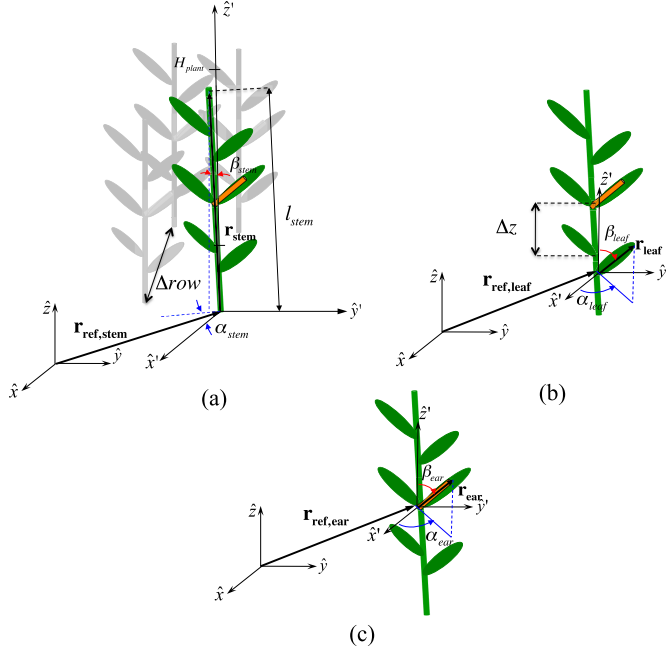| Stage	DAP	Height (cm)	LAI	Vegetation cover (%)	Characteristics
Early	0-38	< 33	< 0.2	<22	Almost bare soil with low vegetation before tasseling
Mid	38-50	$33 - 167$	$0.2 - 2.5$	22-100	Maximum vegetative growth, from tasseling to silking
Late	> 50	$167 - 200$	$2.5 - 2.8$	100	After silking and ear formation

Fig. 3. Contour vectors of the vegetation elements. (a) Stems. (b) Leaves. (c) Ears.

B. Growing Vegetation Contribution

The periodic effects, plant structure, and phenological changes in σ^0_{canopy} are estimated by a specific generator based on field observations [12], [39], [40]. In this phenology-based specific generator, the periodicity in vegetation is represented by a discrete location where the plants can emerge, following the periodicity of the soil (Fig. 1). The plant structure includes leaf vertical distribution on the stems as a Gaussian probability function and the ear height location that is restricted to a specific interval based upon [23]. The relative locations, orientation, length, and width of the plant constituents are modeled as time-variant. These time variations are based upon field observations and the phenological changes of the corn plant (see Table I).

1) Vegetation Representation: The corn plants are represented as one layer that has a specific volume fraction and size distributions for stems, leaves, and ears according to the ground description. Each plant is modeled as a set of cylinders (stems and ears) and blades (leaves).

a) Stem generation: For a realistic representation of corn plants, the generator creates a discrete location of stem along the $\hat{x}$-axis (see Fig. 3). The contour vector for a stem element

(cylindrical element) is defined by [see Fig. 3(a)]

$$\mathbf{r_{stem}} = l_s \cos \alpha_{\text{stem}} \sin \beta_{\text{stem}} \hat{x} + l_s \sin \alpha_{\text{stem}} \sin \beta_s \hat{y}$$
$$+ l_{\text{stem}} \cos \beta_{\text{stem}} \hat{z} + \mathbf{r_{ref,stem}} \quad (17)$$

where $0 < l_s \le l_{\text{stem}}$, $\alpha_{\min} \le \alpha_{\text{stem}} \le \alpha_{\max}$, and $\beta_{\min} \le \beta_{\text{stem}} \le \beta_{\max}$. $\mathbf{r_{ref,stem}}$ is the reference vector for stems, l_{stem} is maximum length for stems, α_{stem} is the azimuthal angle for stems ranging between $\alpha_{\min}$ and $\alpha_{\max}$, and β_{stem} is the tilt angle for stems with maximum and minimum values represented by $\beta_{\max}$ and $\beta_{\min}$, respectively. Maximum and minimum values for these angles are obtained from ground observations, and α_{stem} and β_{stem} follow a uniform distribution. The reference vector for stems is the point on the field where the plant emerges and is given by

$$\mathbf{r_{ref,stem}} = x_{\text{ref,stem}} \hat{x} + y_{\text{ref,stem}} \hat{y}. \quad (18)$$

In this equation, y is a random variable with a uniform distribution ranging between $y_{\max}$ and $y_{\min}$ and $x_{\text{ref,stem}}$ is a discrete variable defined as

$$x_{\text{ref,stem}} = \left\lfloor \frac{x_1}{\Delta\text{row}} \right\rfloor \Delta\text{row} \quad (19)$$

where x_1 is a random variable with a uniform distribution between $x_{\max}$ and $x_{\min}$, Δrow represents the space between rows, and $\lfloor \cdot \rfloor$ is the floor function.

b) Leaf generation: A leaf element starts on a joint point with the stem. If the leaf azimuthal orientation is defined as α_{leaf} and the tilt angle as β_{leaf}, the contour vector for the leaf element is defined by

$$\mathbf{r_{leaf}} = l_l \cos \alpha_{\text{leaf}} \sin \beta_{\text{leaf}} \hat{x} + l_l \sin \alpha_{\text{leaf}} \sin \beta_{\text{leaf}} \hat{y}$$
$$+ l_l \cos \beta_{\text{leaf}} \hat{z} + \mathbf{r_{ref,leaf}} \quad (20)$$

with $0 < l_l \le l_{\text{leaf}}$. The vector $\mathbf{r_{ref,leaf}}$ specifies the node where the leaf attaches to the stem [Fig. 3(b)]. For a single leaf, this vector can be represented as

$$\mathbf{r_{ref,leaf}} = z_{\text{ref,leaf}} \cos \alpha_{\text{stem}} \tan \beta_{\text{stem}} \hat{x}$$
$$+ z_{\text{ref,leaf}} \sin \alpha_{\text{stem}} \tan \beta_{\text{stem}} \hat{y} + z_{\text{ref,leaf}} \hat{z} \quad (21)$$

where $z_{\text{ref,leaf}}$ is a discrete variable with a Gaussian distribution defined by

$$z_{\text{ref,leaf}} = \left\lfloor \frac{z_n - z_0}{\Delta z} \right\rfloor \Delta z + z_0 \quad (22)$$

with z_0 being the height of the bottom leaf on the stem, Δz representing the distance between the nodes where the leaves emerge on the stem, and z_n indicating the height of leaves following a continuous Gaussian distribution with parameters $N(((l_{\text{stem}} + z_0)/2), \sigma_z)$. During the growing season,

l_{leaf}, Δz, z_0, and σ_z vary over time to represent variations in plant structure and phenological changes.

  c) Ear generation: Similar to leaves, ears are also related to the stem by their bottom point. Defining the azimuthal orientation defined as α_{ear} and the tilt angle as β_{ear}, the contour vector for an ear element is defined by

$$\mathbf{r}_{\text{ear}} = l_e \cos\alpha_{\text{ear}} \sin\beta_{\text{ear}}\hat{x} + l_e \sin\alpha_{\text{ear}} \sin\beta_{\text{ear}}\hat{y}$$
$$+ l_e \cos\beta_{\text{ear}}\hat{z} + \mathbf{r}_{\text{ref,ear}} \quad (23)$$

with $0 < l_e \leq l_{\text{ear}}$. The vector $\mathbf{r}_{\text{ref,ear}}$ specifies the node where the ear attaches to the stem [Fig. 3(c)]. For a single ear, this vector can be represented as

$$\mathbf{r}_{\text{ref,ear}} = z_{\text{ref,ear}} \cos\alpha_{\text{stem}} \tan\beta_{\text{stem}}\hat{x}$$
$$+ z_{\text{ref,ear}} \sin\alpha_{\text{stem}} \tan\beta_{\text{stem}}\hat{y} + z_{\text{ref,ear}}\hat{z} \quad (24)$$

where $z_{\text{ref,ear}}$ represents the height where the ear attaches to the stem and is a variable with a uniform distribution ranging between z_{min} and z_{max}. The values of z_{min} and z_{max} depend upon field observations.

  2) Coherent Scattering From the Corn Canopy: To account for the coherent effects due to the plant structure and the row periodicity, we use the distorted Born approximation to evaluate the canopy contribution, similar to [43]–[45]. An equivalent expression to (1) to calculate the backscattering coefficient from a corn field is

$$\sigma^0_{\text{terrain},pq} = \sigma^0_{\text{soil},pq} + \frac{4\pi}{A}|\mathbf{S}_{\text{canopy},pq}|^2 \quad (25)$$

with $\{p,q\}=\{V,H\}$, A is the illuminated area, σ^0_{soil} is the soil contribution as expressed in (15), and $\mathbf{S}_{\text{canopy}}$ is the scattering matrix from the canopy. It is assumed that all the elements are entirely illuminated by a plane wave in a global coordinate system $(\hat{k}_i, \hat{v}_i, \hat{h}_i)$ as defined in (8).

  Neglecting the effect of multiple scattering among the vegetation components (scatterers), $\mathbf{S}_{\text{canopy}}$ can be evaluated from

$$\mathbf{S}_{\text{canopy}} = \sum_{n=1}^{N} e^{j\phi_n}\mathbf{S}_n \quad (26)$$

where N is the total number of scatterers within the canopy, $\mathbf{S}_n$ is the scattering matrix of the nth scatterer, and ϕ_n is the phase compensation term accounting for the shift of the phase reference from the local coordinate system of the nth scatterer to the global coordinate phase reference. Similar to the incident field, the scattered electrical field is considered as propagating in the coordinate system $(\hat{k}_s, \hat{v}_s, \hat{h}_s)$ as defined in (7) and (9). Denoting the position of the nth scatterer in the global coordinate system by $\mathbf{r_n}$, ϕ_n is given by

$$\phi_n = (\hat{k}_i - \hat{k}_s) \cdot \mathbf{r_n}. \quad (27)$$

  Each scatterer (i.e., stems, leaves, and ears) mainly contributes four scattering components, direct scattering ($\mathbf{S}_n^s$), ground–scatterer scattering ($\mathbf{S}_n^{gs}$), scatterer–ground scattering ($\mathbf{S}_n^{sg}$), and ground–scatterer–ground scattering ($\mathbf{S}_n^{gsg}$), as presented in Fig. 4. The scattering matrix $\mathbf{S}_n$ from each
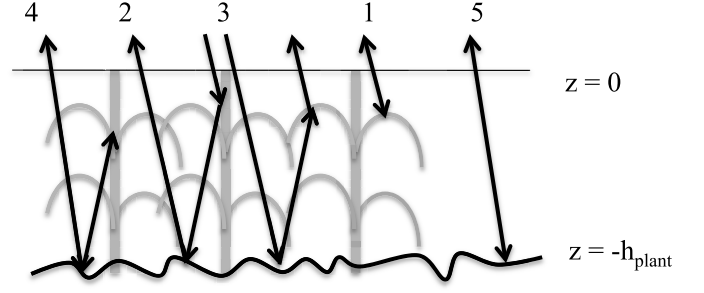
1 : direct vegetation ($\mathbf{S}_n^s$)   5 : direct ground ($\mathbf{S}^{soil}$)
2 : vegetation-ground ($\mathbf{S}_n^{sg}$)
3 : ground-vegetation ($\mathbf{S}_n^{gs}$)
4 : ground-vegetation-ground ($\mathbf{S}_n^{gsg}$)

Fig. 4.   Scattering mechanisms considered in the model. 1: direct vegetation ($\mathbf{S}_n^s$).

vegetation component is obtained by adding coherently these scattering mechanisms

$$\mathbf{S}_n = \mathbf{S}_n^s + \mathbf{S}_n^{gs} + \mathbf{S}_n^{sg} + \mathbf{S}_n^{gsg}. \quad (28)$$

  The scattering mechanisms by each scatterer is obtained by

$$\mathbf{S}_n^s = \mathbf{T}_n^i \cdot \mathbf{S}_n^0(\hat{k}_s, \hat{k}_i) \cdot \mathbf{T}_n^i \quad (29)$$
$$\mathbf{S}_n^{gs} = \mathbf{T}^t \cdot \mathbf{R}(\hat{k}_s, \hat{k}_{gs}) \cdot \mathbf{T}_n^r \cdot \mathbf{S}_n^0(\hat{k}_{gs}, \hat{k}_i) \cdot \mathbf{T}_n^i e^{j\tau_s} \quad (30)$$
$$\mathbf{S}_n^{sg} = \mathbf{T}_n^i \cdot \mathbf{S}_n^0(\hat{k}_s, \hat{k}_{gi}) \cdot \mathbf{T}_n^r \cdot \mathbf{R}(\hat{k}_{gi}, \hat{k}_i) \cdot \mathbf{T}^t e^{j\tau_i} \quad (31)$$
$$\mathbf{S}_n^{gsg} = \mathbf{T}^t \cdot \mathbf{R}(\hat{k}_s, \hat{k}_{gs}) \cdot \mathbf{T}_n^r \cdot \mathbf{S}_n^0(\hat{k}_{gs}, \hat{k}_{gi})$$
$$\cdot \mathbf{T}_n^r \cdot \mathbf{R}(\hat{k}_{gi}, \hat{k}_i) \cdot \mathbf{T}^t e^{j(\tau_i + \tau_s)} \quad (32)$$

with

$$\hat{k}_{gi} = \hat{k}_i - 2\hat{n}_g(\hat{n}_g \cdot \hat{k}_i) \quad (33)$$
$$\hat{k}_{gs} = \hat{k}_s - 2\hat{n}_g(\hat{n}_g \cdot \hat{k}_s) \quad (34)$$
$$\tau_i = 2k_0(\mathbf{r_n} \cdot \hat{n}_g)(\hat{n}_g \cdot \hat{k}_i) \quad (35)$$
$$\tau_s = 2k_0(\mathbf{r_n} \cdot \hat{n}_g)(\hat{n}_g \cdot \hat{k}_s). \quad (36)$$

  In (29)–(36), k_0 is the wavenumber of free space, $\mathbf{S}_n^0$ is the bistatic scattering matrix of the nth scatterer in free space, the incident and scattering directions are denoted by the unit vectors in the argument, $\mathbf{R}$ is the reflection matrix of the dielectric plane whose elements are derived in terms of the Fresnel reflection coefficient [46], $\hat{n}_g$ is the unit vector normal to the flat ground surface, τ_i and τ_s are the phase terms accounting for the extra path lengths due to the reflection on the ground at the incident and scattering directions, and $\mathbf{T}_n^i$, $\mathbf{T}_n^r$, and $\mathbf{T}^t$ are the transmissivity matrices, respectively, for the direct, reflected, and total traveling path.

  The effect of the attenuation and phase change of the coherent wave propagating in the random media, such as vegetation in this paper with high permittivity fluctuations, is modeled by the mean field within random medium using Foldy's approximation [47]. Assuming azimuthal symmetry,

the transmissivity matrices can be obtained by

$$\mathbf{T} = \begin{bmatrix} e^{-jM_{vv}d} & 0 \\ 0 & e^{-jM_{hh}d} \end{bmatrix} \qquad (37)$$

and

$$M_{pq} = \frac{2\pi D}{k_0} \langle S_{pq}^0(\hat{k}_i, \hat{k}_i) \rangle \qquad (38)$$

where D is the volume density of the scatterer and $\langle S_{pq}^0(\hat{k}_i, \hat{k}_i) \rangle$ is the ensemble average of the forward scattering matrix at pq polarization. The path d accounts for the distance between the input and output points of the vegetation layer.

The expressions for the bistatic scattering matrices ($\mathbf{S}_n^0$) for stems and ears are computed using the semiexact solution for the scattered electrical field from a smooth cylinder based on the infinite cylinder approximation [46], and $\mathbf{S}_n^0$ for leaves is obtained by solving the scattered electrical field from a dielectric blade structure [48].

The components σ_{dir}^0 and σ_{int}^0 in (1) can be approximated as

$$\sigma_{\text{dir}}^0 = \frac{4\pi}{A} \left| \sum_{n=1}^{N} e^{j\phi_n} \mathbf{S}_n^s \right|^2 \qquad (39)$$

$$\sigma_{\text{int}}^0 = \frac{4\pi}{A} \left| \sum_{n=1}^{N} e^{j\phi_n} \left(\mathbf{S}_n^{gs} + \mathbf{S}_n^{sg} + \mathbf{S}_n^{gsg} \right) \right|^2. \qquad (40)$$

III. STUDY SITE AND FIELD EXPERIMENTS

MicroWEXs are a series of season-long experiments conducted in the North Central Florida since 2003, to monitor microwave signatures of bare soil and growing vegetation [39], [40], [49], [50]. For this paper, we use observations during the tenth and eleventh MicroWEXs (MicroWEX-10 and MicroWEX-11) in 2011 [39] and 2012 [40], respectively, which were conducted in a 65 m × 75 m field. Data collected during the MicroWEX-11 were used to calibrate the modified coherent model and the MicroWEX-10 database to validate the model. During the two experiments, ground-based active observations were collected simultaneously with measurements of soil and vegetation parameters.

A. Ground-Based Active Observations

The active microwave observations (σ^0) were conducted using UF L-band Automated Radar System (UFLARS) at 1.25-GHz, providing σ^0 of four polarization combinations (HH, VV, HV, and VH) at an unprecedented temporal resolution of every 15 min, day and night [51]. The high-temporal data sets collected by the UFLARS allow for model development and evaluation during hydrologically dynamic conditions. The UFLARS was mounted on a Genie manlift set at a height of 16.2 m and an incidence angle of 40°, resulting in an observation footprint of about 9.8 m × 8.7 m. A single-target calibration technique using a trihedral corner-reflector was applied weekly to obtain quad-pol σ^0 from the received signal. In order to reduce fading in radar measurements, the observations of σ^0 were averaged over measurements obtained spatially along three azimuthal scans at −9°, 0°, and +9°, and nine frequency measurements at 30-MHz increments

from 1130–1370 MHz at each azimuth angle, as obtained from [51]. The overall uncertainty of UFLARS measurements was quantified to be 1.71 dB, as mentioned in [32].

B. Measurements of Soil Parameters

In situ measurements of SM at depths of 2, 4, 8, 16, 32, and 64 cm were obtained using time-domain reflectometry sensors CS616. Based on our previous study [52], we found that the backscattering coefficient at the L-band is highly correlated with SM at depths of 2 and 4 cm. In this paper, we used a plausible near-surface soil (0–5 cm) obtained using a random-forest-based relationship developed between calibrated SM at depths of 2 and 4 cm and soil temperature measured at 2 cm during vegetated periods. This relationship was then applied over the whole growing season to obtain season-long plausible SM [52]. Four rain gauges were used to record the amount of water input during irrigation/precipitation events. A linear move irrigation system was used to maintain uniform water application to the field. Soil roughness measurements, including root-mean-square (rms) height (h_{rms}) and correlation length (*cl*), were obtained using a traditional meshboard method [50]. The 2-D surface profiles, in the directions perpendicular and parallel to the row structure, were measured using a 2-m-long grid board. The surface profile from each grid board was digitized to calculate h_{rms} and *cl*. The soil texture was composed of 89.4% by vol. fine sand and 7.1% by vol. clay.

During the MicroWEX-11, a bare-soil experiment was conducted from May 27 [day of year (DoY) 148], 2012 to June 6 [DoY 158], 2012 prior to planting corn. On DoY 145, a seedless planting was conducted using a multirow cultivator to provide a typical uniform soil roughness during the planting and germination stages. Figs. 5 and 6 show the soil parameters, respectively, for bare-soil conditions in the MicroWEX-11 and during vegetated conditions in the MicroWEX-10 and the MicroWEX-11. The planting day for the MicroWEX-10 was on July 5 (DoY 186), 2011 and for the MicroWEX-11 on August 17 (DoY 230), 2012.

C. Measurements of Vegetation Parameters

The field was disked and planted using a multirow cultivator to make the vegetation density as uniform as possible in the field. For both seasons, the row spacing was 91 cm, with approximately six plants per meter. Weekly destructive vegetation samplings were conducted, including the measurements of vegetation water content, volumetric densities, and geometrical descriptions of vegetation components, such as stems, leaves, and ears, over the two seasons [39], [40]. The MicroWEX-10 was conducted from DoY 186 to 250, 2011 [day after planting (DAP) 0–64] and the MicroWEX-11 from DoY 230 to 297, 2012 (DAP 0–67). The growing seasons of sweet corn were divided into different growth stages as presented in Table I. Fig. 7 presents the vegetation parameters for both the MicroWEX-10 and the MicroWEX-11.

IV. METHODOLOGY

A. Model Calibration

The model was calibrated by estimating the backscatter during the MicroWEX-11. In order to compare model simulations
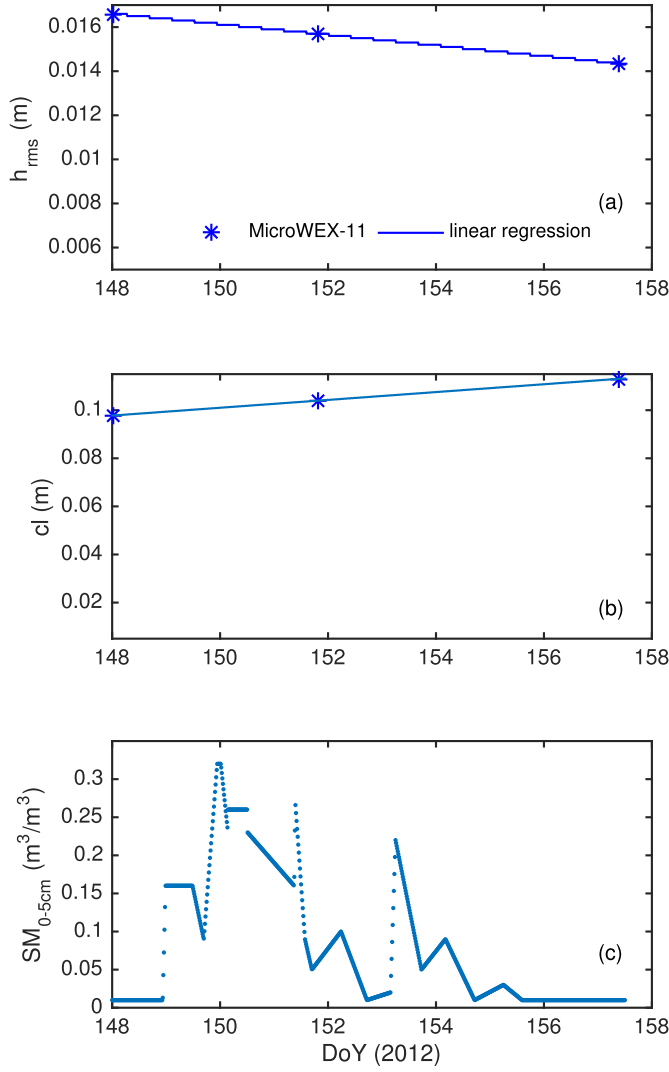
Fig. 5. Soil parameters observed during MicroWEX-11 [40] for bare-soil conditions. The soil parameters are (a) rms height, (b) correlation length, and (c) SM at 0–5 cm.

during the MicroWEX-10 and the MicroWEX-11 for vegetated conditions, we use DAP instead of DoY.

1) Bare-Soil Conditions: In this paper, we estimate σ^0_{soil} for bare soil at 1.25 GHz with an incidence angle of 40° and an exponential correlation function when considering both periodic and random components and considering only the random component as described in Section II-A. We estimate $\sigma^0_{\text{terrain}}$ at VV ($\sigma^0_{\text{terrainVV}}$) and HH ($\sigma^0_{\text{terrainHH}}$) polarizations (pols) for bare-soil conditions, from DoY 148 to 158, 2012, during the MicroWEX-11. For the two-scale surface model and based on field observations, the height profile of the row periodic component of the field site can be represented as

$$Z(x) = -6.36 \times 10^{-8} x^6 + 3.12 \times 10^{-5} x^4$$
$$- 3.45 \times 10^{-3} x^2 + 5.75 \quad (41)$$

with $0 \le x \le T$. Period T corresponds to the space between rows, thus 0.91 m, and x is expressed in meters. In this paper, we assume that profile $Z(x)$ is constant over time. Based on the results shown in [24] for a random soil at the

L-band, the backscattering coefficient at cross-pol from the AIEM model was set constant to −20 dB.

The rms height (h_{rms}), correlation length (cl), and SM values at 0–5 cm for bare-soil conditions observed during the MicroWEX-11 are presented in Fig. 5. The soil permittivities at 0–5 cm were obtained using [53]. The mineralogically based model [53] is widely used for SM retrieval algorithms and has been found to be more applicable than previous models [54], particularly, for the soil consisting in high fraction of sand [52], [55]. The mineralogically based model calculates the soil permittivity based on

$$n_{\text{soil}} = \begin{cases} n_d + (n_b - 1)m_v & m_v \le m_{vt} \\ n_d + (n_b - 1)m_{vt} \\ \quad + (n_f - 1)(m_v - m_{vt}) & m_v > m_{vt} \end{cases}$$

$$k_{\text{soil}} = \begin{cases} k_d + k_b m_v & m_v \le m_{vt} \\ k_d + k_b m_{vt} \\ \quad + k_f(m_v - m_{vt}) & m_v > m_{vt} \end{cases} \quad (42)$$

where n is the refractive index (RI), k is the normalized attenuation coefficient (NAC), the subscripts *soil*, *d*, *b*, and *f* refer to the soil, dry soil, bound water, and free water, m_v is the soil water content, and m_{vt} is the fraction of the maximum bound water. The mineralogically based equations for the RI and NAC of each element mentioned above are formed and listed in [53].

2) Growing Vegetation: We estimate $\sigma^0_{\text{terrainVV}}$ and $\sigma^0_{\text{terrainHH}}$ during the growing season of sweet corn, from DAP 4 to 67, in 2012, during the MicroWEX-11 using the coherent model with the two-scale soil and the specific generator described in Section II and when considering a random soil and a random generator for plants. For both the cases, $\sigma^0_{\text{terrain}}$ was estimated at 1.25 GHz and 40° incidence angle. Parameters describing the soil were obtained by linear interpolation, as shown in Fig. 6, and the parameters from stems, leaves, and ears for this paper were obtained from the MicroWEX-11 and are given in Fig. 7. Vegetation permittivities were estimated using [56].

The equations describing structural and phenological changes for variables z_0, Δz, and σ_z of leaves [see (21)] are

$$z_0 = -2.52 \times 10^{-2} \left(\frac{h_{\text{plant}} - 1.13}{0.62} \right)^3$$
$$- 3.33 \times 10^{-2} \left(\frac{h_{\text{plant}} - 1.13}{0.62} \right)^2$$
$$+ 9.85 \times 10^{-2} \left(\frac{h_{\text{plant}} - 1.13}{0.62} \right) + 0.15 \quad (43)$$

$$\Delta z = -1.11 \times 10^{-2} \left(\frac{h_{\text{plant}} - 1.13}{0.62} \right)^3$$
$$- 2.28 \times 10^{-2} \left(\frac{h_{\text{plant}} - 1.13}{0.62} \right)^2$$
$$+ 4.11 \times 10^{-2} \left(\frac{h_{\text{plant}} - 1.13}{0.62} \right) + 0.11 \quad (44)$$

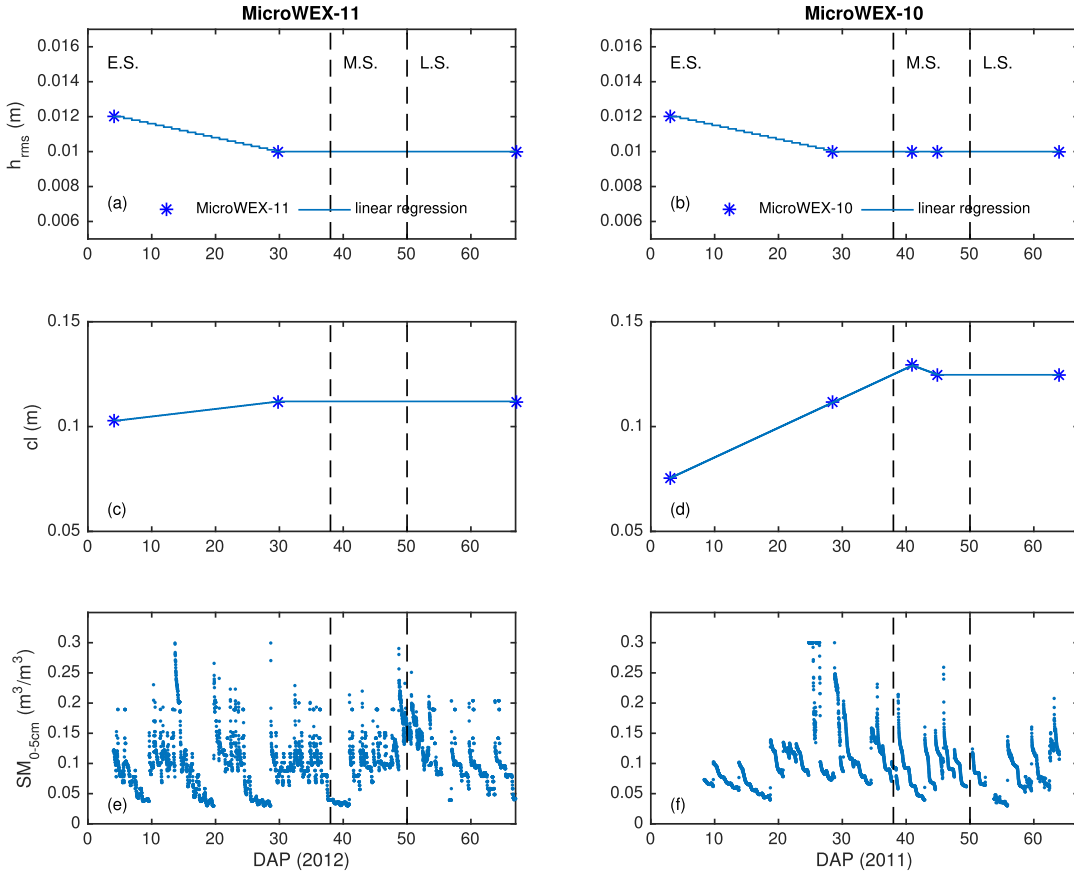$$\sigma_z = 0.53 \left(\frac{h_{\text{plant}}}{2} \right) \quad (45)$$

Fig. 6. Soil parameters observed during MicroWEX-11 [40] and MicroWEX-10 [39] for vegetated conditions. E.S.—early stage. M.S.—midstage. L.S.—late stage. The parameters are (a) and (b) rms height for MicroWEX-11 and MicroWEX-10, (c) and (d) correlation length for MicroWEX-11 and MicroWEX-10, and (e) and (f) SM at 0–5 cm for MicroWEX-11 and MicroWEX-10.

where h_{plant} represents the plant height. Based on field observations, the height of the ear location is restricted to $z \in [25\text{–}48]$ cm.

The average $\sigma_{\text{terrain}}^{0}$ was estimated using the Monte Carlo method with 650 realizations to ensure an oscillation amplitude in $\sigma_{\text{terrain}}^{0} < 0.25$ dB. The results from the simulations are compared with radar observations collected during the MicroWEX-11.

To quantify the combined coherent effects of soil and vegetation rows, phenological changes, and plant structure on the backscattering coefficient, we compare the predictions from the random representation [57] and the specific generation with measurements from the UFLARS collected during the MicroWEX-11. The performance for each of the representations is statistically evaluated by the bias (Bias), the rms difference (RMSD), and the unbiased RMSD (ubRMSD) over the growing season and for each of the growth stages. Bias, RMSD, and ubRMSD are evaluated as

$$\text{Bias} = \frac{\sum_{i=1}^{N_p} \left(\sigma_{pq,i}^{0,\text{model}} - \sigma_{pq,i}^{0,obs} \right)}{N_p} \qquad (46)$$

$$\text{RMSD} = \sqrt{\frac{\sum_{i=1}^{N_p} \left(\sigma_{pq,i}^{0,\text{model}} - \sigma_{pq,i}^{0,obs} \right)^2}{N_p}} \qquad (47)$$

$$\text{ubRMSD} = \sqrt{\text{RMSD}^2 - \text{Bias}^2}. \qquad (48)$$

In these equations, $\sigma_{pq,i}^{0,\text{model}}$ is the predicted backscatter at time i and pq polarization, $\sigma_{pq,i}^{0,obs}$ is the observed backscatter at the same time and polarization, and N_p is the number of $(\sigma_{pq,i}^{0,\text{model}}$ and $\sigma_{pq,i}^{0,obs})$ pairs.

B. Dominant Scattering Mechanisms and Uncertainty Analysis

We identify the dominant scattering mechanisms from each of the vegetation elements contributing to $\sigma_{\text{terrain}}^{0}$ for the growth stages of the MicroWEX-11. To understand the impact of uncertainties of corn parameters on terrain backscatter estimates, we examine time-dependent correlations between the vegetation and soil parameters and the backscattering coefficient. Uncertainty in vegetation parameters was obtained from corn measurements during previous MicroWEXs [39], [40], [49], [50]. The probabilistic density function characterizing the uncertainty for each of the variables in the vegetation and soil description is presented in Table II. The uncertainty in soil parameters can be represented by an additive error, whereas for the vegetation parameters by a multiplicative error [31], [58]. A total of 30 replicates in the open-loop simulation were carried out to achieve the criterion of $\sigma_{\text{terrain}}^{0} < 0.25$ dB in the average value at all polarizations when generating randomly an error for each of the 16 variables at each of the replicates.
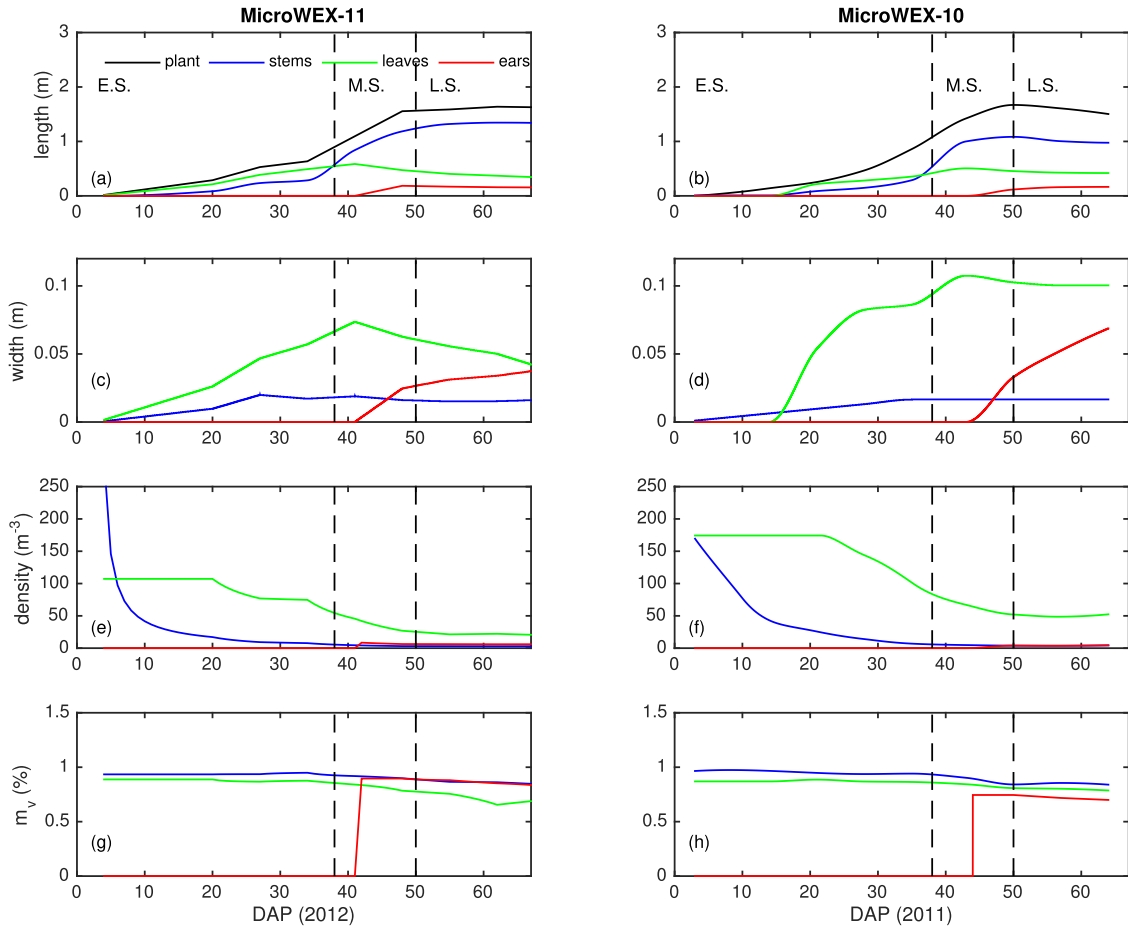
Fig. 7. Vegetation parameters observed during MicroWEX-11 [40] and MicroWEX-10 [39] for vegetated conditions. E.S.—early stage. M.S.—midstage. L.S.—late stage. The parameters are (a) and (b) lengths for the plant, stems, leaves, and ears during MicroWEX-11 and MicroWEX-10, (c) and (d) widths for stems, leaves, and ears during MicroWEX-11 and MicroWEX-10, (e) and (f) volumetric densities for stems, leaves, and ears during MicroWEX-11 and MicroWEX-10, and (g) and (h) water content for stems, leaves, and ears during MicroWEX-11 and MicroWEX-10. The planting day for the MicroWEX-11 was on DoY 230 in 2012 and for the MicroWEX-19 on DoY 186 in 2011.

TABLE II

SOURCES OF UNCERTAINTIES IN THE BACKSCATTERING MODEL. μ AND σ REPRESENT THE MEAN AND STANDARD DEVIATION, RESPECTIVELY

Model parameter	Symbol	Distribution	Distribution parameter
RMS height (cm)	h_{rms}	Additive uniform	0.3
Correlation length (cm)	cl	Additive uniform	3.0
Volumetric soil moisture (m^3/m^3)	SM	Additive uniform	4%
Plant height (m)	h_{plant}	Multiplicative Gaussian	μ=0, σ=10%
Stem length (m)	l_{stem}	Multiplicative Gaussian	μ=0, σ=10%
Leaf length (m)	l_{leaf}	Multiplicative Gaussian	μ=0, σ=35%
Ear length (m)	l_{ear}	Multiplicative Gaussian	μ=0, σ=30%
Stem width (m)	w_{stem}	Multiplicative Gaussian	μ=0, σ=35%
Leaf width (m)	w_{leaf}	Multiplicative Gaussian	μ=0, σ=40%
Ear width (m)	w_{ear}	Multiplicative Gaussian	μ=0, σ=30%
Stem water content (%)	mv_{stem}	Multiplicative Gaussian	μ=0, σ=5%
Leaf water content (%)	mv_{leaf}	Multiplicative Gaussian	μ=0, σ=10%
Ear water content (%)	mv_{ear}	Multiplicative Gaussian	μ=0, σ=20%
Stem density (m^{-3})	D_{stem}	Multiplicative Gaussian	μ=0, σ=20%
Leaf density (m^{-3})	D_{leaf}	Multiplicative Gaussian	μ=0, σ=20%
Ear density (m^{-3})	D_{ear}	Multiplicative Gaussian	μ=0, σ=20%

C. Model Evaluation

The calibrated model was used to estimate backscatter during a second independent season in the MicroWEX-10. The model simulated a backscatter from DAP 3 to 64, 2011, covering a complete growing season of sweet corn. The performance of the model for the MicroWEX-10 is also evaluated using the Bias, the RMSD, and the ubRMSD over the growing season and for each of the growth stages.

V. RESULTS AND DISCUSSION

A. Model Calibration

1) Bare-Soil Conditions: Fig. 8 compares $\sigma^0_{\text{terrainVV}}$ and $\sigma^0_{\text{terrainHH}}$ for bare-soil conditions obtained when considering both the random and periodic components and considering only the random component. There is an averaged difference of 1.6 and 3.5 dB between radar observations and the

TABLE III

BIAS, RMSD, AND ubRMSD BETWEEN THE BACKSCATTER OBSERVATIONS AND THE MODELS USING A RANDOM GENERATOR [57] AND THE PHENOLOGY-BASED GENERATOR PRESENTED IN THIS PAPER FOR THE MicroWEX-11 EXPERIMENT [40] DURING THE GROWING SEASON AND AT EACH GROWTH STAGE OF CORN. B.S., E.S., M.S., AND L.S. REPRESENT THE BARE SOIL, EARLY STAGE, MIDSTAGE, AND LATE STAGE, RESPECTIVELY

| Stage | Model with phenology-based generator | | | | | | Model with random generator | | | | | |
| | Bias (dB) | | RMSD (dB) | | ubRMSD (dB) | | Bias (dB) | | RMSD (dB) | | ubRMSD (dB) | |
	VV	HH	VV	HH	VV	HH	VV	HH	VV	HH	VV	HH
B. S.	1.28	0.93	1.73	1.54	1.16	1.22	2.90	3.33	3.31	3.78	1.58	1.79
Overall	-0.17	1.51	1.58	2.04	1.57	1.37	-0.07	3.41	1.70	3.74	1.70	1.55
E. S.	0.72	1.12	1.29	1.79	1.06	1.39	1.15	4.49	1.63	4.73	1.16	1.48
M. S.	-1.57	1.41	2.02	1.87	1.26	1.23	-1.63	2.72	2.05	2.95	1.24	1.14
L. S.	0.67	2.37	1.10	2.64	0.87	1.16	0.49	2.71	0.99	2.95	0.86	1.14
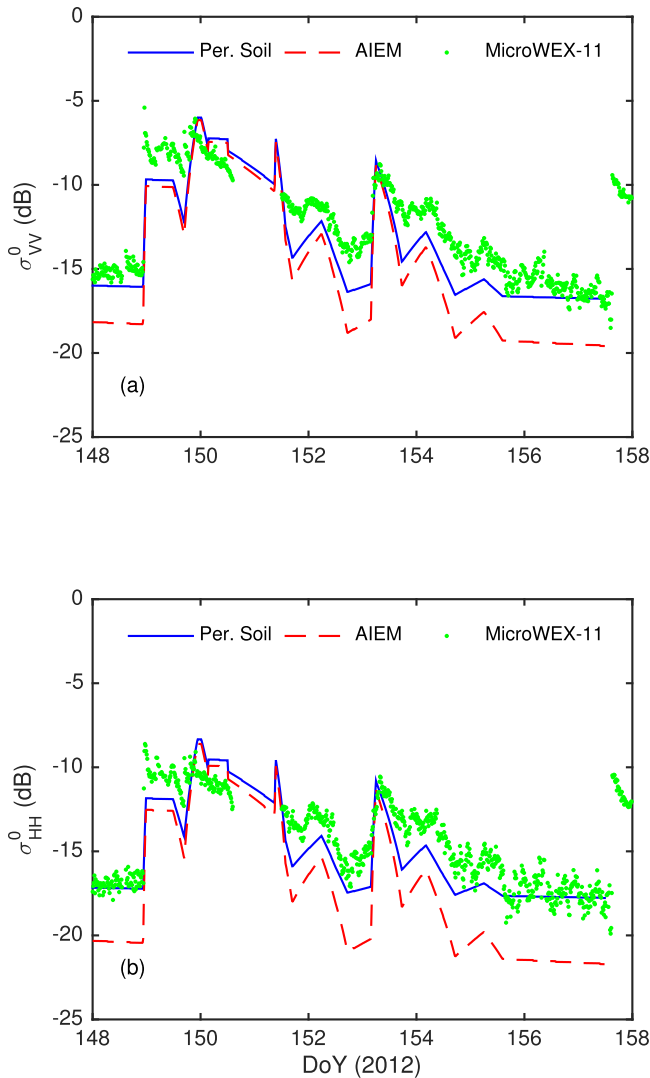
Fig. 8. Comparison of (a) $\sigma^0_{\text{terrainVV}}$ and (b) $\sigma^0_{\text{terrainHH}}$ among backscatter observations and the models considering periodic and random components of the soil (periodic soil, noted as "Per. Soil" in the figure) and only the random component AIEM model during MicroWEX-11 for bare-soil conditions on sandy soil at 40° incidence following the experiment setup described in Section III.

two-component and random-component representations, respectively (see bare-soil conditions in Table III). Similar to [25], the soil representation as a two-component model increases the backscatter up to 2 dB compared with the random-component representation. Major differences between the two soil representations are observed during dry conditions at both co-pols (e.g., see DoY 148–149 and DoY 155.5–158 in Fig. 8). During these periods, the two-component surface model shows a difference of 0.84 and 1.66 dB at VV and HH-pols, respectively, compared with observations. In contrast, the random-component surface model shows a difference of 1.93 and 3.81 dB at VV and HH-pols, respectively, compared with observations. The differences between the two representations decrease as the SM increases. Under dry conditions (no water inputs), the difference between observations and the two soil representations remains almost constant. After removing the bias with observations in both the soil representations, the ubRMSD still remains 0.5 dB higher when considering the random component only compared with the two-component representation (see Table III). This shows that the bias estimation under dry conditions partially compensates for the row effects under rainfall events; thus, a two-component representation of the soil is necessary to account for the row effects and be able to analyze a wider range of SM conditions.

2) Vegetated Conditions:

a) Overall growing season: Fig. 9 compares $\sigma^0_{\text{terrainVV}}$ and $\sigma^0_{\text{terrainHH}}$ from radar observations to those obtained using the two-scale soil and the phenology-based generator for vegetation and the random generator for soil and vegetation [57], henceforth, the random representation, over the growing season in 2012. The model using the phenology-based generator shows lower differences with observations compared with the random representation throughout the growing season. As presented in Table III, both representations show a similar average RMSD of 1.6 dB at VV-pol compared with observations. However, at HH-pol, the random representation shows an RMSD of 3.74 dB with observations, whereas the phenology-based generator shows an RMSD of 2.04 dB. As shown in Fig. 9(b), $\sigma^0_{\text{terrainHH}}$ from the random representation depicts a difference of as much as 8 dB with observations, even under vegetated conditions. In contrast, the maximum difference in $\sigma^0_{\text{terrainHH}}$ between the specific representation and observations is 6 dB. Similar to [27] and [30], both representations show their maximum differences with observations in $\sigma^0_{\text{terrainHH}}$ when the plant is getting closer to its maximum biomass (DAP 53). For $\sigma^0_{\text{terrainVV}}$, after DAP 29, the difference between the two representations is almost negligible. Because of the dominant
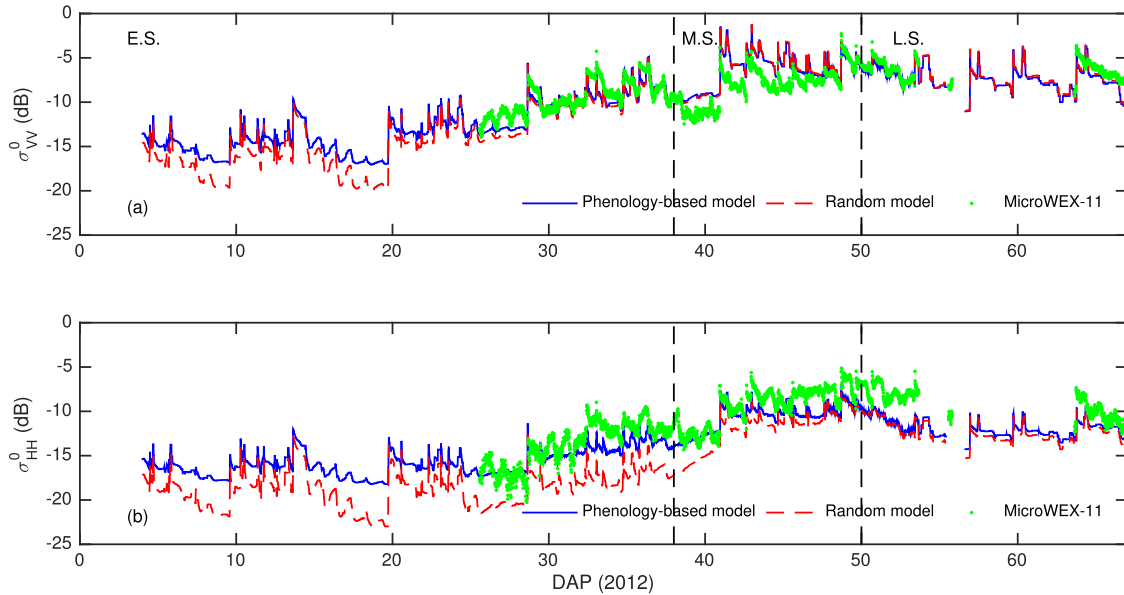
Fig. 9. Comparison of (a) $\sigma^0_{\text{terrainVV}}$ and (b) $\sigma^0_{\text{terrainHH}}$ between backscatter observations and the models considering a periodic generator and a random generator during MicroWEX-11 for vegetated conditions at 40° incidence. E.S.—early stage. M.S.—midstage. L.S.—late stage.

contribution from vegetation at VV-pol, $\sigma^0_{\text{terrainVV}}$ from the two representations overlaps as the plant grows up; however, for $\sigma^0_{\text{terrainHH}}$, the combination of row effects, plant structure, and phenological changes has a major impact, and there is a difference of up to 5.78 dB between the two representations all over the growing season. The bias removal at VV-pol did not reduce the differences with observations for both the representations. In contrast, at HH-pol, the difference is significantly reduced after bias removal for the two representations (see Table III). The ubRMSD between observations and the model with a specific generator is 0.2 dB lower than the difference between the model with a random generator for the two co-pols. For all co-pols, both RMSD and ubRMSD from the model with the specific representation are similar to the uncertainty in radar observations (1.71 dB).

b) Early stage: At the beginning of the experiment, the behavior observed between the two representations of the corn is similar to that for the bare-soil conditions, prior to planting. Once the corn plant emerges (DAP 5), the difference in $\sigma^0_{\text{terrainVV}}$ between the two representations gradually decreases and the two representations overlap on DAP 29 [see Fig. 9(a)] when the plant reaches a height of 60 cm, with about 35 leaves/m² (a maximum number of leaves). After this day, the leaves become wider but the number of leaves per m² does not vary significantly. For the period when the radar observations were available (from DAP 26), the model with the phenology-based generator shows an RMSD of 1.29 dB with observations, whereas the model with a random generator depicts an RMSD of 1.63 dB (see Table III). For $\sigma^0_{\text{terrainHH}}$, the RMSD is 1.79 and 4.73 dB for the specific representation and the random representation, respectively, compared with field observations. $\sigma^0_{\text{terrainHH}}$ from the phenology-based representation is higher than that from the random representation, reaching a difference of up to 5 dB. This shows that the estimates of $\sigma^0_{\text{terrainHH}}$ are strongly affected when the combined

effects of rows, plant structure, and phenological changes are neglected, even during the early stage of the plant.

c) Midstage: During this stage, both the representations overestimate $\sigma^0_{\text{terrainVV}}$ and underestimate $\sigma^0_{\text{terrainHH}}$ (Fig. 9). Unlike the model with a random generator, the statistical parameters (RMSD, Bias, and ubRMSD) of the model with a specific generator are always similar to the uncertainty in the radar observations (see Table III). During this period, the corn crop reached its maximum biomass and, after DAP 41, there are continuous rainfalls. These conditions may be causing the differences between the estimates of $\sigma^0_{\text{terrain}}$ and radar observations. At VV-pol, radar observations show a faster drydown than the estimations of $\sigma^0_{\text{terrainVV}}$ do. SM sensors indicate additional water inputs (small rainfalls) that the radar does not capture (see Figs. 6 and 9 from DAP 41 to 44.5). At HH-pol, radar observations suggest a constant rainfall from DAP 45 to 48; in contrast, $\sigma^0_{\text{terrainHH}}$ from the models show drydown intervals compared with the observed SM. This behavior may indicate periods of standing water on the upper leaves of the plant that is not observed by the SM sensors and VV-pol radar observations.

d) Late stage: During this stage, in addition to the stem and leaf contributions, the vegetation component also includes contribution from ears. As a result, the vegetation component increases and both the specific and random representations become closer (see Fig. 9). At VV-pol, the Bias, RMSD, and ubRMSD for the two representations are lower than uncertainty in radar observations (see Table III). At HH-pol, during wet conditions, $\sigma^0_{\text{terrainHH}}$ from the two representations are very close; however, during dry conditions, the difference between the two representations increases up to 1.2 dB. Similar to the midstage, at the beginning of the late stage, the HH-pol observations remain abnormally very high after rainfall events, and there is a difference of about 4 dB with the modeled $\sigma^0_{\text{terrainHH}}$ from the two representations.
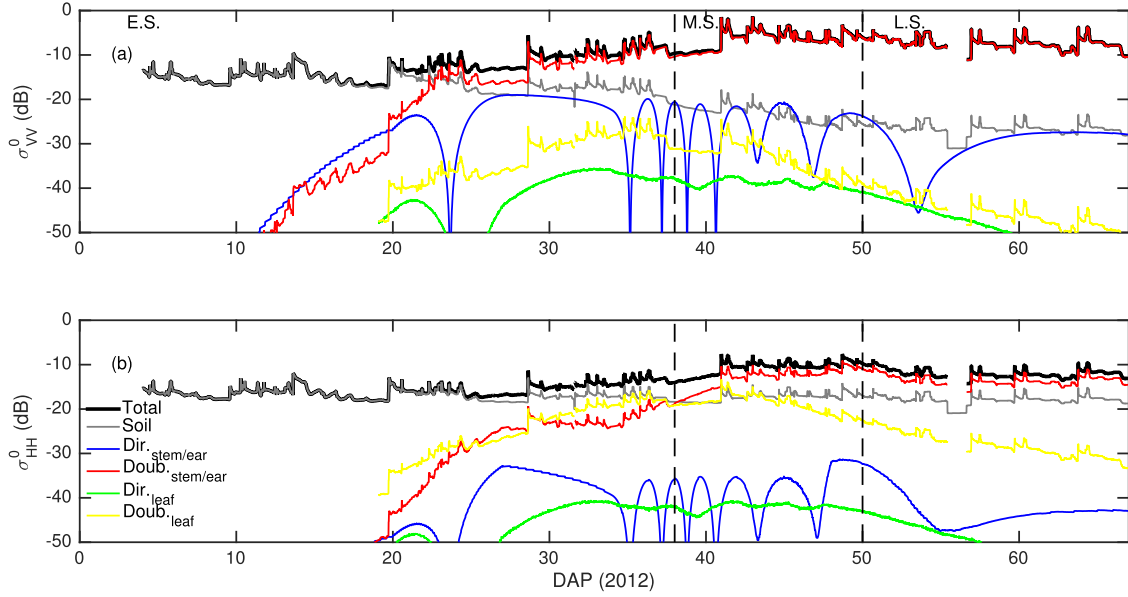
Fig. 10.   Scattering mechanisms from stems, leaves, and ears during MicroWEX-11 for vegetated conditions at (a) VV- and (b) HH-polarizations and 40° incidence according to the model with a periodic generator, following the contributions presented in (49). The ears appeared on DAP 42. E.S.—early stage. M.S.—midstage. L.S.—late stage.

B. Dominant Scattering Mechanism

Considering the different scattering mechanisms presented in (1) and the vegetation elements described in Section II-B, $\sigma_{terrain}^0$ can be expressed as

$$\sigma_{terrain}^0 = \begin{cases} \sigma_{soil}^0 + \sigma_{stem,dir}^0 \\ \quad + \sigma_{leaf,dir}^0 + \sigma_{stem,int}^0 \qquad DAP \leq 42 \\ \quad + \sigma_{leaf,int}^0 \\ \sigma_{soil}^0 + \sigma_{stem/ear,dir}^0 \\ \quad + \sigma_{leaf,dir}^0 + \sigma_{stem/ear,int}^0 \quad DAP > 42 \text{ (ears)} \\ \quad + \sigma_{leaf,int}^0 \end{cases} \qquad (49)$$

where $\sigma_{stem,dir}^0$ and $\sigma_{stem,int}^0$ are the direct scattering from stems and from interactions between stems and soil, respectively, and $\sigma_{leaf,dir}^0$ and $\sigma_{leaf,int}^0$ represent the direct scattering from leaves and from the interactions between leaves and soil, respectively. After DAP 42 (late stage that includes ear formation), the components $\sigma_{stem,dir}^0$ and $\sigma_{stem,int}^0$ include also the contribution from ears, henceforth, $\sigma_{stem/ear,dir}^0$ and $\sigma_{stem/ear,dir}^0$. Fig. 10 shows the contribution of each term in (49) by the model with the two-scale soil representation and the phenology-based generator for vegetation.

1) Early Stage: The σ_{soil}^0 is the main contributor at the beginning of the early stage at both the co-pols. As the crop increases, σ_{soil}^0 gradually decreases its relative contribution. At VV-pol, $\sigma_{stem,int}^0$ becomes the dominant contribution on DAP 24 when the stems reach their maximum length. Because $\sigma_{stem,dir}^0$ is single scattering from a set of cylindrical vegetation elements, it presents large oscillations, as shown in Fig. 10. This is a typical behavior that has also been shown in previous studies, such as [46], [59], and [60]. From DAP 35 to 39, $\sigma_{stem,int}^0$, $\sigma_{leaf,int}^0$, and σ_{soil}^0 are equally dominant at HH-pol. During these days, the corn reaches its maximum biomass.

2) Midstage: During the midstage, $\sigma_{stem,int}^0$ is the dominant contribution at both co-pols. At VV-pol, $\sigma_{stem,int}^0$ is about 18 dB higher than $\sigma_{stem,dir}^0$ and σ_{soil}^0 and about 25 dB higher than leaf contributions, $\sigma_{leaf,dir}^0$ and $\sigma_{leaf,int}^0$. At this stage, the structure from stems dominates the scattering mechanisms at VV-pol. The incorporation of relative location and the phenological changes in leaves do not change the dominant contributor in $\sigma_{terrainVV}^0$. At HH-pol, $\sigma_{stem,int}^0$ is about 5 dB higher than $\sigma_{leaf,int}^0$ and σ_{soil}^0. At this polarization, $\sigma_{leaf,int}^0$ and σ_{soil}^0 are about 9 dB higher compared with VV-pol. The row effects in the soil component and the phenology-based representation of leaves have a higher impact at HH-pol than at VV-pol. Regarding the scattering mechanism [see (1)], the interaction component, σ_{int}^0, is the major contribution as the plant grows up. Compared with $\sigma_{stem,dir}^0$ and $\sigma_{leaf,dir}^0$, $\sigma_{stem,int}^0$ and $\sigma_{leaf,int}^0$ increase their relative contribution and their combined contribution become dominant during the midstage. Once the bottom leaves begin drying (DAP 46), the green biomass from leaves reduces and $\sigma_{leaf,int}^0$ gradually decreases but the interaction scattering mechanism still remains dominant.

3) Late Stage: During the late stage, the ears also contribute to the vegetation–soil interactions and $\sigma_{stem/ear,int}^0$ increases its relative contribution to $\sigma_{terrain}^0$ at both the co-pols. The attenuation due to the vegetation layer also increases, and σ_{soil}^0 reduces its contribution compared with the other two growth stages. For this stage, Monsivais-Huertero and Judge [23] found oscillations due to the random location of ears. The incorporation of restrictions in the ear location removes these oscillations and the $\sigma_{stem/ear,dir}^0$ and $\sigma_{stem/ear,int}^0$ components show a convergent behavior (see Fig. 10).

In general, when including the effects of rows, plant structure, and phenological changes in the modeling, the relative contribution of $\sigma_{leaf,int}^0$ and $\sigma_{stem,int}^0$ to $\sigma_{terrain}^0$ at both the

TABLE IV

CORRELATION COEFFICIENT BETWEEN THE BACKSCATTERING COEFFICIENT AT VV- AND HH-POLS AND PARAMETERS DESCRIBING THE SOIL
AND VEGETATION DURING THE GROWING SEASON AND AT EACH GROWTH STAGE OF CORN FOR THE MicroWEX-11 EXPERIMENT.
B.S., E.S., M.S., AND L.S. REPRESENT THE BARE SOIL, EARLY STAGE, MIDSTAGE, AND LATE STAGE, RESPECTIVELY

Parameter	Overall VV	Overall HH	B.S. VV	B.S. HH	E.S. VV	E.S. HH	M.S. VV	M.S. HH	L.S. VV	L.S. HH
h_{rms}	0.30	0.30	0.66	0.68	0.38	0.40	0.12	0.15	0.24	0.17
cl	0.23	0.21	0.42	0.43	0.30	0.24	0.18	0.09	0.09	0.19
SM	0.22	0.32	0.71	0.69	0.29	0.50	0.13	0.09	0.07	0.11
h_{plant}	0.08	0.03	—	—	0.10	0.05	0.10	0.03	0.03	0.02
l_{stem}	0.14	0.23	—	—	0.17	0.28	0.11	0.24	0.09	0.16
l_{leaf}	0.12	0.13	—	—	0.14	0.19	0.08	0.09	0.09	0.06
l_{ear}	0.04	0.10	—	—	—	—	0.04	0.07	0.03	0.10
w_{stem}	0.22	0.43	—	—	0.22	0.19	0.14	0.54	0.28	0.80
w_{leaf}	0.14	0.23	—	—	0.08	0.28	0.14	0.23	0.25	0.19
w_{ear}	0.40	0.18	—	—	—	—	0.47	0.35	0.37	0.09
mv_{stem}	0.28	0.13	—	—	0.27	0.15	0.32	0.20	0.29	0.04
mv_{leaf}	0.08	0.05	—	—	0.06	0.06	0.09	0.03	0.10	0.02
mv_{ear}	0.06	0.25	—	—	—	—	0.09	0.38	0.04	0.18
D_{stem}	0.15	0.13	—	—	0.07	0.10	0.18	0.16	0.29	0.16
D_{leaf}	0.08	0.12	—	—	0.06	0.18	0.07	0.12	0.13	0.04
D_{ear}	0.16	0.12	—	—	—	—	0.12	0.18	0.19	0.09

co-pols increases compared with results reported in previous studies [23], [30]. At VV-pol, the row representation in both soil and vegetation increases the coherent effects in the interactions between soil and stems compared with a random representation of the field. Similar to [32], most of the specificities in the plant structure and phenological information are related to the relative location of leaves on the plant and result in constructive interferences when the incident waves interact with the leaves, affecting primarily HH-pol. σ_{int}^0 has been reported as the dominant scattering mechanism in different studies using a coherent approach [23], [27], [30], [61]. However, as presented in Section V-A2, a phenology-based generator helps in reducing the difference with radar observations compared with a random representation, even when both the models use a coherent approach. The relative contribution from σ_{soil}^0, $\sigma_{stem/ear,int}^0$, and $\sigma_{leaf,int}^0$ plays an important role in reducing the difference with observations at both the co-pols. However, the accuracy of these estimates varies depending upon the parameterization in the description of stems, leaves, and ears and the representation of the soil. Section V-C is focused on analyzing the uncertainty in the description of these parameters and their effects on the estimates of $\sigma_{terrain}^0$ when taking into account the effects of rows, plant structure, and phenological changes in the modeling.

C. Sensitivity of $\sigma_{terrain}^0$ to the Parameters Describing Soil and Vegetation

We calculate the sensitivity of $\sigma_{terrain}^0$ estimated by the model using the phenology-based generator to uncertainties in the inputs describing the soil and vegetation, as parameterized in Table II, during the MicroWEX-11. Table IV shows that the mean values of the correlation coefficients between $\sigma_{terrainVV}^0$ and $\sigma_{terrainHH}^0$ lead to variations in each of the input parameters for the entire growing season and for each stage of growth. As shown in Fig. 11, variations in soil and vegetation parameters produce variations in $\sigma_{terrain}^0$ of 0.4–3.5 dB. Major uncertainties happen during midseason and late season (from DAP 38) and under rainfall conditions.

Under bare-soil conditions, $\sigma_{terrain}^0$ is very sensitive to SM and h_{rms} at both the co-pols with a correlation coefficient of 0.70 and 0.67, respectively. However, during the growing season, the sensitivity to SM and h_{rms} decreased to 0.40 and 0.39, respectively. For vegetation, the most sensitive parameters are w_{ear} at VV-pol and w_{stem} at HH-pol with correlation coefficients of 0.40 and 0.43, respectively.

During the early stage, SM, h_{rms}, l_{stem}, w_{leaf}, and mv_{stem} are the most sensitive parameters. The VV-pol is equally sensitive to soil and vegetation parameters, whereas HH-pol is mainly sensitive to soil parameters. $\sigma_{terrain}^0$ is still sensitive to SM because of the high contribution from σ_{soil}^0, particularly at HH-pol and, as the plant grows up, σ_{soil}^0 reduces its relative contribution and σ_{int}^0 increases its contribution. While σ_{soil}^0 is highly dependent on SM, σ_{int}^0 is dependent on both the SM and vegetation parameters.

For midstage and late stage, the sensitivity of $\sigma_{terrain}^0$ to soil parameters significantly decreases, reaching values of about 0.12 in the correlation coefficient. At this stage, the most sensitive parameters are related to stems and ears. The stems increase their water content at the height where the ears are located [62] and the leaf contribution decreases. Most of water content in the plant is concentrated in ears and stems, and this increases the double scattering contribution due to interactions of stems and ears with the soil.

The $\sigma_{terrain}^0$ was the most sensitive to SM and rms height and the widths of stems, leaves, and ears, and the stem water content. Parameters, such as leaf area index (LAI) and total biomass, could be used to represent phenological changes in stems, ears, and leaves; however, it is important to account for the row effects in soil and vegetation and the plant structure when using simplified representations, such as the water cloud model, in order to represent realistically the contribution of σ_{int}^0.

D. Model Validation

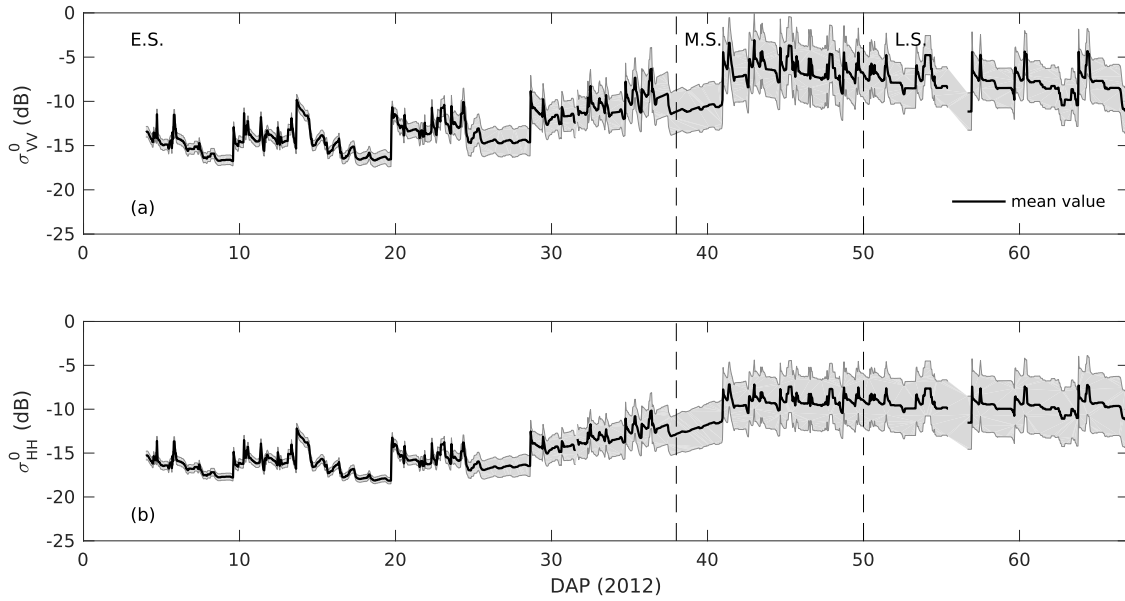The performance of the coherent model using the phenology-based generator was validated for a second growing

Fig. 11. Time series of the uncertainty in (a) $\sigma^0_{\text{terrainVV}}$ and (b) $\sigma^0_{\text{terrainHH}}$ due to uncertainty in the soil and vegetation parameters at 40° incidence.
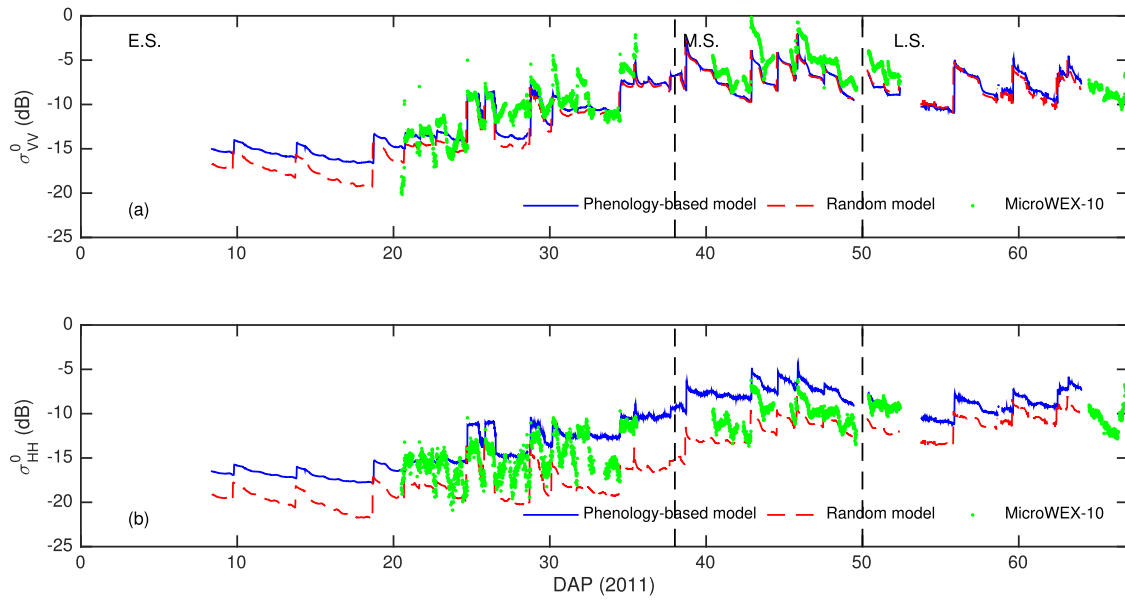

Fig. 12. Comparison of (a) $\sigma^0_{\text{terrainVV}}$ and (b) $\sigma^0_{\text{terrainHH}}$ between backscatter observations and the model considering a periodic generator during MicroWEX-10 for vegetated conditions at 40° incidence. E.S.—early stage. M.S.—midstage. L.S.—late stage.

season of corn. Fig. 12 compares $\sigma^0_{\text{terrainVV}}$ and $\sigma^0_{\text{terrainHH}}$ from the radar observations to those obtained by the model during the MicroWEX-10. The differences between observed and model estimates at both the co-pols are similar to those found during the MicroWEX-11 (compare Figs. 9 and 12). In addition, during both experiments, the lower RMSD is obtained at VV-pol. As presented in Table V, $\sigma^0_{\text{terrainVV}}$ has an RMSD and an ubRMSD of 1.89 and 1.50 dB, respectively, and $\sigma^0_{\text{terrainHH}}$ has an RMSD and an ubRMSD of 2.42 and 1.47 dB, respectively. These values of RMSD and ubRMSD at both the co-pols are very similar to those presented in Table III. However, for the midseason and late season, the model estimates and observations are very close during the

MicroWEX-10, as compared with the MicroWEX-11. During the MicroWEX-10, there were wetter conditions compared with the MicroWEX-11. These conditions increased the sensitivity of $\sigma^0_{\text{terrainVV}}$ and $\sigma^0_{\text{terrainHH}}$ to SM.

During the early season of the MicroWEX-10, the model estimates the similar amplitudes of $\sigma^0_{\text{terrainVV}}$ to observations for both dry and wet conditions. For $\sigma^0_{\text{terrainHH}}$, the model matches observations under wet conditions; however, the model estimates are higher than those observed under dry conditions. Since the main contribution comes from the soil, the pattern should follow SM; however, the high values in $\sigma^0_{\text{terrainHH}}$ do not correspond to rainfall events.

TABLE V

BIAS, RMSD, AND ubRMSD BETWEEN THE BACKSCATTER
OBSERVATIONS AND THE MODEL USING THE PHENOLOGY-
BASED GENERATOR FOR THE MicroWEX-10
EXPERIMENT [39] DURING THE GROWING
SEASON AND AT EACH GROWTH STAGE
OF CORN. E.S., M.S., AND L.S.
REPRESENT THE EARLY STAGE,
MIDSTAGE, AND LATE
STAGE, RESPECTIVELY

Stage	Bias (dB)		RMSD (dB)		ubRMSD (dB)	
	VV	HH	VV	HH	VV	HH
Overall	1.15	-1.93	1.89	2.42	1.50	1.47
E. S.	0.67	-1.73	1.78	2.32	1.65	1.55
M. S.	1.77	-2.74	1.99	2.87	0.91	0.85
L. S.	2.18	-0.27	2.22	0.55	0.45	0.47

During the midseason, the model underestimates $\sigma^0_{\text{terrainVV}}$ and overestimates $\sigma^0_{\text{terrainHH}}$ compared with the MicroWEX-10 observations. However, comparing Figs. 9 and 12 shows opposite behavior during the MicroWEX-11 between DAP 38 and 50. The leaf biomass was higher for this growing season compared with the MicroWEX-11 (see Fig. 7). This results in a higher leaf contribution, $\sigma^0_{\text{leaf}} = \sigma^0_{\text{leaf,dir}} + \sigma^0_{\text{leaf,int}}$. Among the leaf parameters, we found that the width was the parameter that increased the most due to a higher factional cover of leaves, and the bare-soil fraction is reduced. This results in an increase of σ^0_{leaf}.

During the early reproductive stage, when the ears begin contributing to $\sigma^0_{\text{terrain}}$, model estimates have similar RMSD and ubRMSD to the MicroWEX-11 experiment (see Tables III and V) and comparable to the uncertainties in field observations at both co-pols. This demonstrates that the model captures the effects from rows, plant structure, and phenology under high biomass.

VI. CONCLUSION

In this paper, we develop a coherent model to understand the combined effects from periodicity in soil and vegetation rows, the plant structure, and phenological changes during the growing season on the terrain backscatter. In addition to the rms height and the correlation length to describe the random component of soil roughness, the periodicity of the soil surface due to row effects is described by the height profile of the rows. The location of leaves and ears on the plant and of stems in the rows is obtained from statistical parameterizations based upon field observations. The model was calibrated using field observations of vegetation and soil conditions during the sweet corn season in North Central Florida from the MicroWEX-11 and evaluated using season-long observations from the MicroWEX-10. Under bare-soil conditions, it was found that a two-component representation (periodic and random) of soil is necessary to obtain the realistic estimates of the backscatter from agricultural soils under a wide range of SM conditions. The ubRMSD reduced from 3 to 1 dB after accounting for the row effects. The HH-pol was more sensitive than VV-pol to row effects, particularly, during dry conditions.

During vegetated period, HH-pol was more affected than VV-pol when neglecting row effects, plant structure, and

phenological changes on the backscatter. During the early season, the phenology-based model reduced the ubRMSD between model and observations from 5 to 2 dB when compared with the existing random generator-based models. For midseason, $\sigma^0_{\text{terrainVV}}$ was overestimated, whereas $\sigma^0_{\text{terrainHH}}$ was underestimated compared with observations. However, the RSMDs at both the co-pols remained similar to the uncertainty in the radar observations. The RSMDs could be due to frequent irrigation/precipitation events that would cause periods of standing water on the upper leaves. During the late season, both the co-pols observed maximum differences of 1 dB during very dry conditions. When the effects of rows, plant structure, and phenological changes were included in the model, the relative contributions of $\sigma^0_{\text{leaf,int}}$ and $\sigma^0_{\text{stem,int}}$ increased, and as a result, the coherent effects in the interactions between soil and stems also increased compared with a random representation of the field. The relative location of leaves on the plant resulted in constructive interferences when the incident waves interact with the leaves, affecting primarily HH-pol. Thus, combined effects of rows, plant structure, and phenology cannot be compensated by bias correction/removal factors in agricultural regions.

$\sigma^0_{\text{terrain}}$ was the most sensitive to SM and the rms height and widths of stems, leaves, and ears, and the stem water content. Parameters such as LAI and total biomass could be used to represent phenological changes in stems, ears, and leaves; however, it is important to account for the row effects in soil and vegetation and plant structure when using simplified representations, such as the water cloud model, in order to represent realistically the contribution of σ^0_{int}. This paper demonstrates that it is necessary to include periodicity and plant structural effects in algorithms to retrieve realistic SM in agricultural terrain.

REFERENCES

[1] H. McNairn and B. Brisco, "The application of C-band polarimetric SAR for agriculture: A review," *Can. J. Remote Sens.*, vol. 30, no. 3, pp. 525–542, 2004.

[2] S. C. Steele-Dunne, H. McNairn, A. Monsivais-Huertero, J. Judge, P.-W. Liu, and K. Papathanassiou, "Radar remote sensing of agricultural canopies: A review," *IEEE J. Sel. Topics Appl. Earth Observ. Remote Sens.*, vol. 10, no. 5, pp. 2249–2273, May 2017.

[3] A. Rosenqvist *et al.*, "Operational performance of the ALOS global systematic acquisition strategy and observation plans for ALOS-2 PALSAR-2," *Remote Sens. Environ.*, vol. 155, pp. 3–12, Dec. 2014.

[4] Y. Kankaku, S. Suzuki, and M. Shimada, "ALOS-2 first year operation result," in *Proc. IEEE Int. Geosc. Remote Sens. Symp. (IGARSS)*, Jul. 2015, pp. 4121–4124.

[5] Y. Kankaku, S. Suzuki, T. Motohka, M. Ohki, R. Natsuaki, and M. Shimada, "ALOS-2 operation status," in *Proc. IEEE Int. Geosc. Remote Sens. Symp. (IGARSS)*, Jul. 2016, pp. 3846–3848.

[6] Y. H. Kerr, P. Waldteufel, J. P. Wigneron, J. Martinuzzi, J. Font, and M. Berger, "Soil moisture retrieval from space: The Soil Moisture and Ocean Salinity (SMOS) mission," *IEEE Trans. Geosci. Remote Sens.*, vol. 39, no. 8, pp. 1729–1735, Aug. 2001.

[7] D. Entekhabi *et al.*, "The Soil Moisture Active/Passive Mission (SMAP)," in *Proc. IEEE Int. Geosc. Remote Sens. Symp. (IGARSS)*, Jul. 2008, pp. III-1–III-4.

[8] D. Dadamia *et al.*, "Generating a synthetic data base of polarimetric signatures to exploit SAOCOM observations over Pampas," in *Proc. IEEE Int. Geosc. Remote Sens. Symp. (IGARSS)*, Jul. 2015, pp. 267–270.

[9] P. Rosen *et al.*, "The NASA-ISRO SAR mission—An international space partnership for science and societal benefit," in *Proc. IEEE Radar Conf. (RadarCon)*, May 2015, pp. 1610–1613, doi: 10.1109/RADAR.2015.7131255.

[10] S. Chakrabarti, T. Bongiovanni, J. Judge, K. Nagarajan, and J. C. Principe, "Downscaling satellite-based soil moisture in heterogeneous regions using high-resolution remote sensing products and information theory: A synthetic study," *IEEE Trans. Geosci. Remote Sens.*, vol. 53, no. 1, pp. 85–101, Jan. 2015.

[11] N. N. Das, D. Entekhabi, R. S. Dunbar, E. G. Njoku, and S. H. Yueh, "Uncertainty estimates in the SMAP combined active–passive downscaled brightness temperature," *IEEE Trans. Geosci. Remote Sens.*, vol. 54, no. 2, pp. 640–650, Feb. 2016.

[12] P.-W. Liu, J. Judge, R. D. De Roo, A. W. England, and T. Bongiovanni, "Uncertainty in soil moisture retrievals using the SMAP combined active–passive algorithm for growing sweet corn," *IEEE J. Sel. Topics Appl. Earth Observ. Remote Sens.*, vol. 9, no. 7, pp. 3326–3339, Jul. 2016.

[13] X. Wu, J. P. Walker, C. Rüdiger, R. Panciera, and Y. Gao, "Intercomparison of alternate soil moisture downscaling algorithms using active–passive microwave observations," *IEEE Geosci. Remote Sens. Lett.*, vol. 14, no. 2, pp. 179–183, Feb. 2017.

[14] A. Monsivais-Huertero, I. Chenerie, and K. Sarabandi, "Estimation of sahelian-grassland parameters using a coherent scattering model and a genetic algorithm," *IEEE Trans. Geosci. Remote Sens.*, vol. 47, no. 4, pp. 999–1011, Apr. 2009.

[15] C. Montzka *et al.*, "Investigation of SMAP fusion algorithms with airborne active and passive L-band microwave remote sensing," *IEEE Trans. Geosci. Remote Sens.*, vol. 54, no. 7, pp. 3878–3889, Jul. 2016.

[16] R. Akbar, M. H. Cosh, P. E. O'Neill, D. Entekhabi, and M. Moghaddam, "Combined radar–radiometer surface soil moisture and roughness estimation," *IEEE Trans. Geosci. Remote Sens.*, vol. 55, no. 7, pp. 4098–4110, Jul. 2017, doi: 10.1109/TGRS.2017.2688403.

[17] F. Chen *et al.*, "Application of triple collocation in ground-based validation of soil moisture active/passive (SMAP) Level 2 data products," *IEEE J. Sel. Topics Appl. Earth Observ. Remote Sens.*, vol. 10, no. 2, pp. 489–502, Feb. 2017.

[18] S.-B. Kim *et al.*, "Surface soil moisture retrieval using the l-band synthetic aperture radar onboard the Soil Moisture Active–Passive satellite and evaluation at core validation sites," *IEEE Trans. Geosci. Remote Sens.*, vol. 55, no. 4, pp. 1897–1914, Apr. 2017.

[19] S. C. Dunne, D. Entekhabi, and E. G. Njoku, "Impact of multiresolution active and passive microwave measurements on soil moisture estimation using the ensemble Kalman smoother," *IEEE Trans. Geosci. Remote Sens.*, vol. 45, no. 4, pp. 1016–1028, Apr. 2007.

[20] K. Nagarajan, J. Judge, A. Monsivais-Huertero, and W. D. Graham, "Impact of assimilating passive microwave observations on root-zone soil moisture under dynamic vegetation conditions," *IEEE Trans. Geosci. Remote Sens.*, vol. 50, no. 11, pp. 4279–4291, Nov. 2012.

[21] A. Monsivais-Huertero, J. Judge, S. Steele-Dunne, and P. Liu, "Impact of bias correction methods on estimation of soil moisture when assimilating active and passive microwave observations," *IEEE Trans. Geosci. Remote Sens.*, vol. 54, no. 1, pp. 262–278, Jan. 2016.

[22] P.-W. Liu *et al.*, "Assimilation of active and passive microwave observations for improved estimates of soil moisture and crop growth," *IEEE J. Sel. Topics Appl. Earth Observ. Remote Sens.*, vol. 9, no. 4, pp. 1357–1369, Apr. 2016.

[23] A. Monsivais-Huertero and J. Judge, "Comparison of backscattering models at L-band for growing corn," *IEEE Geosci. Remote Sens. Lett.*, vol. 8, no. 1, pp. 24–28, Jan. 2011.

[24] M. W. Whitt and F. T. Ulaby, "Radar response of periodic vegetation canopies," *Int. J. Remote Sens.*, vol. 15, no. 9, pp. 1813–1848, 1994.

[25] M. Zribi, O. Taconet, V. Ciarletti, and D. Vidal-Madjar, "Effect of row structures on radar microwave measurements over soil surface," *Int. J. Remote Sens.*, vol. 23, no. 24, pp. 5211–5224, 2002.

[26] A. Tavakoli, K. Sarabandi, and F. T. Ulaby, "Horizontal propagation through periodic vegetation canopies," *IEEE Trans. Antennas Propag.*, vol. 39, no. 7, pp. 1014–1023, Jul. 1991.

[27] J. M. Stiles, K. Sarabandi, and F. T. Ulaby, "Electromagnetic scattering from grassland. II. Measurement and modeling results," *IEEE Trans. Geosci. Remote Sens.*, vol. 38, no. 1, pp. 349–356, Jan. 2000.

[28] L. He *et al.*, "Influence of row wheat on radar backscatter for azimuthal look angles at L-, S-, C-, and X-bands," *IEEE Geosci. Remote Sens. Lett.*, vol. 13, no. 6, pp. 811–815, Jun. 2016.

[29] K. Sarabandi, A. Tavakoli, and F. T. Ulaby, "Propagation in a two-dimensional periodic random medium with inhomogeneous particle distribution," *IEEE Trans. Antennas Propag.*, vol. 40, no. 10, pp. 1175–1186, Oct. 1992.

[30] N. S. Chauhan, D. M. Le Vine, and R. H. Lang, "Discrete scatter model for microwave radar and radiometer response to corn: Comparison of theory and data," *IEEE Trans. Geosci. Remote Sens.*, vol. 32, no. 2, pp. 416–426, Mar. 1994.

[31] Y. Liu, K.-S. Chen, P. Xu, and Z.-L. Li, "Modeling and characteristics of microwave backscattering from rice canopy over growth stages," *IEEE Trans. Geosci. Remote Sens.*, vol. 54, no. 11, pp. 6757–6770, Nov. 2016.

[32] P.-W. Liu, J. Judge, R. D. DeRoo, A. W. England, T. Bongiovanni, and A. Luke, "Dominant backscattering mechanisms at L-band during dynamic soil moisture conditions for sandy soils," *Remote Sens. Environ.*, vol. 178, pp. 104–112, Jun. 2016.

[33] A. T. Joseph, R. van der Velde, P. E. O'Neill, R. H. Lang, and T. Gish, "Soil moisture retrieval during a corn growth cycle using L-band (1.6 GHz) radar observations," *IEEE Trans. Geosci. Remote Sens.*, vol. 46, no. 8, pp. 2365–2374, Aug. 2008.

[34] M. Hosseini, H. McNairn, A. Merzouki, and A. Pacheco, "Estimation of Leaf Area Index (LAI) in corn and soybeans using multi-polarization C- and L-band radar data," *Remote Sens. Environ.*, vol. 170, pp. 77–89, Dec. 2015.

[35] J. Ma *et al.*, "Estimating vegetation water content of corn and soybean using different polarization ratios based on L- and S-band radar data," *IEEE Geosci. Remote Sens. Lett.*, vol. 14, no. 3, pp. 364–368, Mar. 2017.

[36] X. Jiao, H. McNairn, J. Shang, E. Pattey, J. Liu, and C. Champagne, "The sensitivity of Radarsat-2 polarimetric SAR data to corn and soybean leaf area index," *Can. J. Remote Sens.*, vol. 37, no. 1, pp. 69–81, 2011.

[37] A. T. Joseph, R. van der Velde, P. E. O'Neill, R. Lang, and T. Gish, "Effects of corn on C- and L-band radar backscatter: A correction method for soil moisture retrieval," *Remote Sens. Environ.*, vol. 114, no. 11, pp. 2417–2430, 2010.

[38] S.-B. Kim, M. Moghaddam, L. Tsang, M. Burgin, X. Xu, and E. G. Njoku, "Models of L-band radar backscattering coefficients over global terrain for soil moisture retrieval," *IEEE Trans. Geosci. Remote Sens.*, vol. 52, no. 2, pp. 1381–1396, Feb. 2014.

[39] T. Bongiovanni *et al.*, "Field observations during the tenth microwave water and energy balance experiment (MicroWEX-10): From March 1, 2011 through January 5, 2012," Center Remote Sens., Univ. Florida, Gainesville, FL, USA, Tech. Rep. AE512, 2015. [Online]. Available: http://edis.ifas.ufl.edu/ae512

[40] T. Bongiovanni *et al.*, "Field observations during the eleventh microwave water and energy balance experiment (MicroWEX-11): From Apr. 25, 2012 through December, 2012," Center Remote Sens., Univ. Florida, Tech. Rep. AE514, 2015. [Online]. Available: http://edis.ifas.ufl.edu/ae514

[41] A. K. Fung, Z. Li, and K. S. Chen, "Backscattering from a randomly rough dielectric surface," *IEEE Trans. Geosci. Remote Sens.*, vol. 30, no. 2, pp. 356–369, Mar. 1992.

[42] T. D. Wu, K. S. Chen, J. Shi, H. W. Lee, and A. K. Fung, "A study of an AIEM model for bistatic scattering from randomly rough surfaces," *IEEE Trans. Geosci. Remote Sens.*, vol. 46, no. 9, pp. 2584–2598, Sep. 2008.

[43] R. H. Lang and J. S. Sighu, "Electromagnetic backscattering from a layer of vegetation: A discrete approach," *IEEE Trans. Geosci. Remote Sens.*, vol. GRS-21, no. 1, pp. 62–71, Jan. 1983.

[44] A. Sharma and R. H. Lang, "Small scale surface roughness effects on enhanced backscatter from a layer of vegetation," in *Proc. USNC-URSI Radio Sci. Meeting (Joint AP-S Symp.)*, Jul. 2017, pp. 59–60.

[45] H. Huang *et al.*, "Modelling and validation of combined active and passive microwave remote sensing of agricultural vegetation at L-band," *Progr. Electromagn. Res. B*, vol. 78, pp. 91–124, 2017, doi: 10.2528/PIERB17060303.

[46] F. T. Ulaby and C. Elachi, *Radar Polarimetry for Geoscience Applications*. Norwood, MA, USA: Artech House, 1990.

[47] L. Tsang, J. Kong, and R. Shin, *Theory of Microwave Remote Sensing*. New York, NY, USA: Wiley, 1985.

[48] J. M. Stiles, K. Sarabandi, and F. T. Ulaby, "Microwave scattering model for grass blade structures," *IEEE Trans. Geosci. Remote Sens.*, vol. 31, no. 5, pp. 1051–1059, Sep. 1993.

[49] J. Casanova et al., "Field observations during the fifth microwave, water, and energy balance experiment (MicroWEX-5): From March 9 through May, 2006," Circular no. 1514, Center Remote Sens., Univ. Florida, Gainesville, FL, USA, Tech. Rep. AE407, 2006. [Online]. Available: http://edis.ifas.ufl.edu/AE407

[50] M. Yang, K. Calvin, J. Casanova, and J. Judge, "Measurements of soil surface roughness during the fourth microwave water and energy balance experiment: Apr. 18 through June 13, 2005," Center Remote Sens., Univ. Florida, Tech. Rep. AE363, 2005. [Online]. Available: http://edis.ifas.ufl.edu/AE363

[51] K. Nagarajan et al., "Automated L-band radar system for sensing soil moisture at high temporal resolution," *IEEE Geosci. Remote Sens. Lett.*, vol. 11, no. 2, pp. 504–508, Feb. 2014.

[52] P.-W. Liu, R. D. De Roo, A. W. England, and J. Judge, "Impact of moisture distribution within the sensing depth on L- and C-band emission in sandy soils," *IEEE J. Sel. Topics Appl. Earth Observ. Remote Sens.*, vol. 6, no. 2, pp. 887–899, Apr. 2013.

[53] V. L. Mironov, L. G. Kosolapova, and S. V. Fomin, "Physically and mineralogically based spectroscopic dielectric model for moist soils," *IEEE Trans. Geosci. Remote Sens.*, vol. 47, no. 7, pp. 2059–2070, Jul. 2009.

[54] J.-P. Wigneron et al., "Evaluating an improved parameterization of the soil emission in L-MEB," *IEEE Trans. Geosci. Remote Sens.*, vol. 49, no. 4, pp. 1177–1189, Sep. 2011.

[55] Y. H. Kerr et al., "The SMOS soil moisture retrieval algorithm," *IEEE Trans. Geosci. Remote Sens.*, vol. 50, no. 5, pp. 1384–1403, May 2012.

[56] F. T. Ulaby and M. A. El-Rayes, "Microwave dielectric spectrum of vegetation—Part II: Dual-dispersion model," *IEEE Trans. Geosci. Remote Sens.*, vol. GRS-25, no. 5, pp. 550–557, Sep. 1987.

[57] A. Monsivais-Huertero, K. Sarabandi, and I. Chenerie, "Multipolarization microwave scattering model for sahelian grassland," *IEEE Trans. Geosci. Remote Sens.*, vol. 48, no. 3, pp. 1416–1432, Mar. 2010.

[58] G. Cookmartin, P. Saich, S. Quegan, R. Cordey, P. Burgess-Allen, and A. Sowter, "Modeling microwave interactions with crops and comparison with ERS-2 SAR observations," *IEEE Trans. Geosci. Remote Sens.*, vol. 38, no. 2, pp. 658–670, Mar. 2000.

[59] T. Chiu and K. Sarabandi, "Electromagnetic scattering interaction between a dielectric cylinder and a slightly rough surface," *IEEE Trans. Antennas Propag.*, vol. 47, no. 5, pp. 902–913, May 1999.

[60] H. Huang, L. Tsang, E. G. Njoku, A. Colliander, T.-H. Liao, and K.-H. Ding, "Propagation and scattering by a layer of randomly distributed dielectric cylinders using Monte Carlo simulations of 3D Maxwell equations with applications in microwave interactions with vegetation," *IEEE Access*, vol. 5, pp. 11985–12003, 2017.

[61] H. Huang et al., "Coherent model of L-band radar scattering by soybean plants: Model development, evaluation, and retrieval," *IEEE J. Sel. Topics Appl. Earth Observ. Remote Sens.*, vol. 9, no. 1, pp. 272–284, Jan. 2016.

[62] J. J. Casanova, J. Judge, and M. Jang, "Modeling transmission of microwaves through dynamic vegetation," *IEEE Trans. Geosci. Remote Sens.*, vol. 45, no. 10, pp. 3145–3149, Oct. 2007.

Alejandro Monsivais-Huertero (S'06–M'07–SM'13) received the B.S. degree in telecommunications engineering from the National Autonomous University of Mexico, Mexico City, Mexico, in 2002, and the M.S. degree in microwaves and optical telecommunications and the Ph.D. degree in microwaves, electromagnetism, and optoelectronics from the University of Toulouse, Toulouse, France, in 2004 and 2007, respectively.

From 2004 to 2006, he was with the Antennes, Dispositifs et Matériaux Microondes Laboratory, University of Toulouse, and from 2006 to 2007, he was with the Laboratoire d'Etudes et de Recherche en Imagerie Spatiale et Médicale, University of Toulouse. From 2008 to 2009, he was a Post-Doctoral Research Associate with the Center for Remote Sensing, Department of Agricultural and Biological Engineering, University of Florida, Gainesville. Since 2010, he has been a Researcher with the Escuela Superior de Ingenieria Mecanica y Electrica campus Ticoman, Instituto Politecnico Nacional, Mexico City. His research interests include microwave and millimeter-wave radar remote sensing, electromagnetic wave propagation, and retrieval algorithms.

Pang-Wei Liu (S'09–M'13) received the Ph.D. degree in agricultural engineering (minor in electrical engineering) from the University of Florida, Gainesville, FL, USA, in 2013.

He was a Post-Doctoral Research Associate and then an Assistant Research Scientist with the Center for Remote Sensing, Institute of Food and Agricultural Sciences, University of Florida. He is currently a Post-Doctoral Scholar with the Jet Propulsion Laboratory, National Aeronautics and Space Administration, California Institute of Technology, Pasadena, CA, USA. His research interests include active and passive microwave remote sensing modeling for soil moisture and agricultural crops under dynamic vegetation conditions, data assimilation with crop growth models, hydrology modeling using land information system, the application of LiDAR for forest biomass, and GNSS-R remote sensing for terrestrial applications.

Dr. Liu is a member of the IEEE Geoscience and Remote Sensing Society and the American Geophysical Union.

Jasmeet Judge (S'94–M'00–SM'05) received the Ph.D. degree in electrical engineering and atmospheric, oceanic, and space sciences from the University of Michigan, Ann Arbor, MI, USA, in 1999.

She is currently an Associate Professor with the Department of Agricultural and Biological Engineering, Institute of Food and Agricultural Sciences, University of Florida, Gainesville, FL, USA, where she is also the Director of the Center for Remote Sensing. Her research interests include microwave remote-sensing applications to terrestrial hydrology for dynamic vegetation; modeling of energy and moisture interactions at the land surface and in the vadose zone; spatial and temporal scaling of remotely sensed observations in heterogeneous landscapes; and data assimilation.

Dr. Judge is a member of the Frequency Allocations in Remote Sensing Technical Committee in the IEEE Geoscience and Remote Sensing Society. She is the Chair of the National Academies' Committee on Radio Frequencies. She also serves the American Geophysical Union as the past Chair of the Remote Sensing Technical Committee in the Hydrology Section.